The Monitor project: rotation of low-mass stars in the open cluster NGC 2516

Jonathan Irwin,[1]* Simon Hodgkin,[1] Suzanne Aigrain,[1] Leslie Hebb,[2] Jerome Bouvier,[3] Cathie Clarke,[1] Estelle Moraux[3] and D. M. Bramich[4]

[1]*Institute of Astronomy, University of Cambridge, Madingley Road, Cambridge CB3 0HA*
[2]*School of Physics and Astronomy, University of St Andrews, North Haugh, St Andrews KY16 9SS*
[3]*Laboratoire d'Astrophysique, Observatoire de Grenoble, BP 53, F-38041 Grenoble Cédex 9, France*
[4]*Isaac Newton Group of Telescopes, Apartado de Correos 321, E-38700 Santa Cruz de la Palma, Canary Islands, Spain*

ABSTRACT

We report on the results of an *i*-band time-series photometric survey of NGC 2516 using the Cerro Tololo Inter-American Observatory (CTIO) 4-m Blanco telescope and 8k Mosaic-II detector, achieving better than 1 per cent photometric precision per data point over $15 \lesssim i \lesssim 19$. Candidate cluster members were selected from a V versus $V - I$ colour–magnitude diagram over $16 < V < 26$ (covering masses from $0.7\,M_\odot$ down to below the brown dwarf limit), finding 1685 candidates, of which we expect $\sim$1000 to be real cluster members, taking into account contamination from the field (which is most severe at the extremes of our mass range). Searching for periodic variations in these gave 362 detections over the mass range $0.15 \lesssim M/M_\odot \lesssim 0.7$. The rotation period distributions were found to show a remarkable morphology as a function of mass, with the fastest rotators bounded by $P > 0.25$ d, and the slowest rotators for $M \lesssim 0.5\,M_\odot$ bounded by a line of $P \propto M^3$, with those for $M \gtrsim 0.5\,M_\odot$ following a flatter relation closer to $P \sim$ constant. Models of the rotational evolution were investigated, finding that the evolution of the fastest rotators was well reproduced by a conventional solid body model with a mass-dependent saturation velocity, whereas core–envelope decoupling was needed to reproduce the evolution of the slowest rotators. None of our models were able to simultaneously reproduce the behaviour of both populations.

Key words: techniques: photometric – surveys – stars: rotation – open clusters and associations: individual: NGC 2516.

1 INTRODUCTION

NGC 2516 is a well-studied nearby intermediate-age open cluster ($\sim$150 Myr; Jeffries, Thurston & Hambly 2001), at a distance modulus $(M - m)_0 = 7.93 \pm 0.14$ (Terndrup et al. 2002). The canonical reddening along the line of sight to the cluster is $E(B - V) = 0.12$, implying a photometrically derived metallicity of $[Fe/H] = -0.05 \pm 0.14$ (Terndrup et al. 2002). The same authors derive a spectroscopic metallicity from two stars of $[Fe/H] = 0.01 \pm 0.03$, consistent within the errors, and implying a slightly larger distance modulus $(M - m)_0 = 8.05 \pm 0.11$. We have adopted the smaller distance modulus of $(M - m)_0 = 7.93 \pm 0.14$ and photometric metallicity for the remainder of this work, but any differences induced in the results by the uncertainty in distance modulus are nevertheless small.

NGC 2516 has often been referred to as the 'Southern Pleiades' owing to its similarity both in angular extent and age, where we adopt an age of 100 Myr (Meynet, Mermilliod & Maeder 1993) for the Pleiades, using the classical main-sequence turnoff ages throughout this work for consistency with the estimate for NGC 2516. The Pleiades metallicity is very similar, at $[Fe/H] = -0.034 \pm 0.024$ (Boesgaard & Friel 1990). Clusters in the age range between α Persei ($\sim$50 Myr, e.g. Basri & Martín 1999) and the Hyades ($\sim$625 Myr, Perryman et al. 1998) are important for constraining stellar evolution models. Fig. 1 shows a plot of the age at which a solar metallicity star reaches the zero-age main-sequence (ZAMS) as a function of stellar mass, indicating that solar mass stars reach the ZAMS at $\sim$40 Myr, and $\sim$0.4–0.5 $M_\odot$ stars reach the ZAMS at the age of NGC 2516. It is therefore highly useful in this regard owing to both its age and relative proximity, where we can study solar mass stars after evolving for a short time on the main sequence, and lower mass stars as they finish pre-main-sequence evolution. The similarity in age to the Pleiades (modulo the uncertainty in this parameter) means that
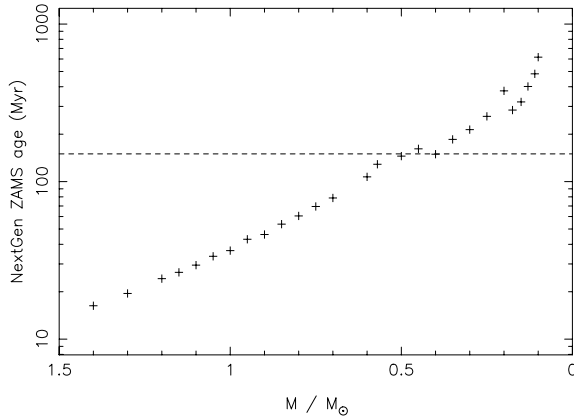
Figure 1. Plot of the approximate age at which the ZAMS is reached for solar metallicity stars, from the NextGen models (Baraffe et al. 1998), computed as the time taken for the star to reach within 1 per cent of its 1-Gyr age radius. The horizontal dashed line indicates the approximate 150-Myr age of NGC 2516.

comparisons of these clusters could be used to study the dependence of stellar parameters on environment.

NGC 2516 is very well studied in the literature. The most relevant existing work includes membership surveys (Jeffries et al. 2001; Sung et al. 2002), characterization of the mass function from solar mass (Jeffries et al. 2001) down to the brown dwarf regime (Moraux, Bouvier & Clarke 2005), a survey for radial velocities and binarity at the bright end of the cluster sequence (González & Lapasset 2000) and studies of rotation using $v \sin i$ covering stars down to G spectral types (Jeffries, James & Thurston 1998; Terndrup et al. 2002). A number of X-ray surveys, including monitoring for variability, have also been carried out (e.g. Sciortino et al. 2001; Damiani et al. 2003; Ramsay, Harra & Kay 2003; Wolk et al. 2004), the most recent of which (Pillitteri et al. 2006) used a deep *XMM–Newton* observation to probe the low-mass members (down to $\sim$ M5) of the cluster. They found that NGC 2516 stars are less luminous in X-rays than the Pleiades members, and suggest that this may be attributed to slightly older age, or lower rotation rates.

1.1 Evolution of stellar angular momentum

For a discussion of the context of this work, the reader is referred to our M34 publication in Irwin et al. (2006). The present survey probes a different open cluster of slightly younger age ($\sim$150 Myr for NGC 2516, compared to $\sim$200 Myr for M34). Because of the small distance modulus and our use of a larger telescope, the NGC 2516 survey probes lower masses, covering a range of $0.1 \lesssim M/M_\odot \lesssim 0.7$, compared to $0.25 \lesssim M/M_\odot \lesssim 1.0$ in M34, allowing the very low-mass stars to be examined in much greater detail. This will allow models of angular momentum evolution to be tested over a wider range of stellar mass, in particular to determine whether models incorporating solid body rotation (e.g. Bouvier, Forestini & Allain 1997) are able to reproduce the observed low-mass angular momentum evolution. At the lowest masses, core-envelope decoupling should not be relevant, since all the stars will be fully convective and thus rotate approximately as solid bodies, allowing us to constrain directly the angular momentum loss law without needing to consider the details of internal angular momentum transport. At the age of NGC 2516, stars with masses $M \lesssim 0.4\,M_\odot$ should be fully convective (Chabrier & Baraffe 1997).

1.2 The survey

We have undertaken a photometric survey in NGC 2516 using the Cerro Tololo Inter-American Observatory (CTIO) 4-m Blanco telescope and Mosaic-II imager. Our goals are twofold: first, to study rotation periods for a sample of low-mass members, covering M spectral types, down to $\sim$0.1 M$_\odot$, and second, to look for eclipsing binary systems containing low-mass stars, to obtain dynamical mass measurements in conjunction with radial velocities from follow-up spectroscopy. Such systems provide the most accurate determinations of fundamental stellar parameters (in particular, masses) for input to models of stellar evolution, which are poorly constrained in this age range. We defer discussion of our eclipsing binary candidates to a later paper once we have obtained suitable follow-up spectroscopy.

These observations are part of a larger photometric monitoring survey of young open clusters over a range of ages and metallicities (the Monitor project; Hodgkin et al. 2006; Aigrain et al. 2007).

The remainder of the paper is structured as follows: the observations and data reduction are described in Section 2, and the colour–magnitude diagram (CMD) of the cluster and candidate membership selection are presented in Section 3. The method we use for obtaining photometric periods is summarized in Section 4 (see Irwin et al. 2006 for a more detailed discussion), and our results are summarized in Section 5. We discuss the implications of these results in Section 6, and our conclusions are summarized in Section 7.

In several of the following sections, we use mass and radius estimates for the cluster members. We note here that these were derived from the 150 Myr NextGen models, using the *I*-band magnitudes, rather than $V - I$ colour or V magnitude, for reasons discussed in Section 3.1.

2 OBSERVATIONS AND DATA REDUCTION

Photometric monitoring observations were obtained using the 4-m CTIO Blanco telescope, with the Mosaic-II imager, during two four-night observing runs, separated by $\sim$1 week, in 2006 February–March. This instrument provides a field of view of $\sim$36 × 36 arcmin^2 (0.37 deg^2), using a mosaic of eight 2k × 4k pixel CCDs, at a scale of $\sim$0.27 arcsec pixel^{-1}. NGC 2516 was observed for $\sim$8 h per night.

In order to maximize the number of cluster members covered by our survey, and given the large angular extent of NGC 2516, we used three fields, with a single 75-s *i*-band exposure in each, observed by cycling around all three fields, to give a cadence of $\sim$9 min, covering $\sim$1 deg^2 of the cluster (illustrated in Fig. 2). Our fields were chosen to be outside the central few arcmin of the cluster to avoid contamination of the images from a number of very bright ($V \sim$ 5–8) stars close to the cluster centre.

The observing conditions were superb, with exceptional seeing ($<$0.8 arcsec on a few nights) and $\sim$6 photometric nights. We also obtained a number of longer *V*-band exposures in photometric conditions (3 × 300 s in each field) to generate a CMD. Our observations are sufficient to give 1 per cent or better photometric precision pre-data point from saturation at $i \sim$ 15 down to $i \sim$ 19 (see Fig. 3), covering early- to mid-M spectral types at the age and distance of NGC 2516.

For a full description of our data reduction steps, the reader is referred to Irwin et al. (2007). Briefly, we used the pipeline for the Isaac Newton Telescope (INT) Wide Field Survey (Irwin & Lewis 2001) for two-dimensional (2D) instrumental signature removal (cross-talk correction, bias correction, flat-fielding) and astrometric and photometric calibration. We then generated the *master catalogue* for
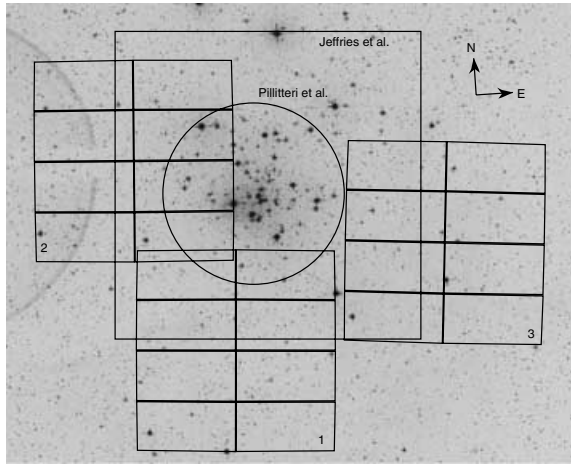
Figure 2. Digitized Sky Survey (DSS) image of NGC 2516 covering $\sim 1°8 \times 1°5$, centred on $07^h57^m25^s$, $-60°55'00''$ (J2000), showing the coverage of the present survey (numbered 8-chip mosaic tiles), the XMM survey of Pillitteri et al. (2006) and the optical survey of Jeffries et al. (2001).
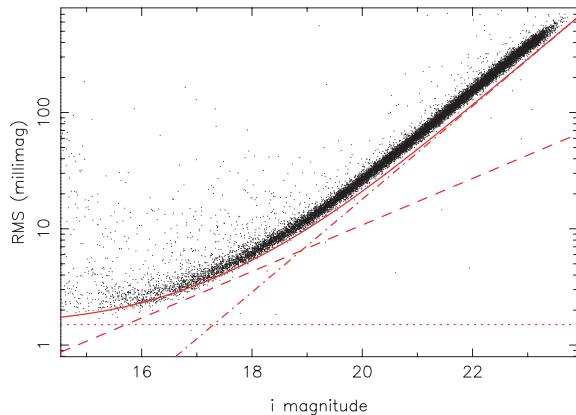

Figure 3. Plot of rms scatter as a function of magnitude for the *i*-band observations of a single field in NGC 2516, for all unblended objects with stellar morphological classifications. The diagonal dashed line shows the expected rms from Poisson noise in the object, the diagonal dot–dashed line shows the rms from sky noise in the photometric aperture and the dotted line shows an additional 1.5 mmag contribution added in quadrature to account for systematic effects. The solid line shows the overall predicted rms, combining these contributions.

each filter by stacking 20 of the frames taken in the best conditions (seeing, sky brightness and transparency) and running the source detection software on the stacked image. The resulting source positions were used to perform aperture photometry on all of the time-series images. We achieved a per data point photometric precision of ~ 2–4 mmag for the brightest objects, with rms scatter <1 per cent for $i \lesssim 19$ (see Fig. 3).

Our source detection software flags as likely blends any objects detected as having overlapping isophotes. This information is used, in conjunction with a morphological image classification flag also generated by the pipeline software (Irwin & Lewis 2001) to allow us to identify non-stellar or blended objects in the time-series photometry.

Photometric calibration of our data was carried out using regular observations of Landolt (1992) equatorial standard star fields in the usual way.

Light curves were extracted from the data for $\sim 100\,000$ objects, $63\,000$ of which had stellar morphological classifications, using our standard aperture photometry techniques, described in Irwin et al. (2007). We fit a 2D quadratic polynomial to the residuals in each frame (measured for each object as the difference between its magnitude on the frame in question and the median calculated across all frames) as a function of position, for each of the eight CCDs separately. Subsequent removal of this function accounted for effects such as varying differential atmospheric extinction across each frame. Over a single CCD, the spatially varying part of the correction remains small, typically ~ 0.02 mag peak-to-peak. The reasons for using this technique are discussed in more detail in Irwin et al. (2007).

For the production of deep CMDs, we stacked 20 *i*-band observations, taken in good seeing and photometric conditions. The limiting magnitudes, measured as the approximate magnitude at which our catalogues are 50 per cent complete (see Section 3.2) on these images were $V \simeq 24.3$ and $i \simeq 22.7$.

3 SELECTION OF CANDIDATE LOW-MASS MEMBERS

Catalogues of photometrically selected candidate members were available from Jeffries et al. (2001) for solar mass down to $\sim 0.2\,M_\odot$ and for ~ 0.2–$0.05\,M_\odot$ from Moraux et al. (2005), but we elected to perform a new photometric selection using *V* versus $V - I$ CMDs from our data, to match exactly the field of view and magnitude range of our time-series photometry. Unfortunately, since we have avoided the very centre of the cluster in our field selection to reduce the effect of saturated bright stars on our CCD frames, the overlap in sky coverage between the present survey and many of the previous ones (e.g. Jeffries et al. 2001; Pillitteri et al. 2006) is relatively poor.

3.1 The *V* versus $V - I$ CMD

Our CMD of NGC 2516 is shown in Fig. 4. The *V* and *i* measurements were converted to the standard Johnson–Cousins photometric system using colour equations derived from our standard star observations:

$$(V - I) = (V_{ccd} - i_{ccd})/0.899, \tag{1}$$

$$V = V_{ccd} + 0.005(V - I), \tag{2}$$

$$I = i_{ccd} - 0.096(V - I). \tag{3}$$

Candidate cluster members were selected by defining an empirical main sequence 'by eye' to follow the clearly visible cluster single-star sequence. The cuts were defined by moving this line along a vector perpendicular to the cluster sequence, by amounts $k - \sigma(V - I)$ and $k + \sigma(V - I)$ as measured along this vector, where $\sigma(V - I)$ is the photometric error in the $V - I$ colour. The values of k used were -0.15 mag for the lower line and 0.5 mag for the upper line on the diagram, making the brighter region wider to avoid rejecting binary and multiple systems, which are overluminous for their colour compared to single stars. 1685 candidate photometric members were selected, over the full *V* magnitude range from $V = 15.5$ to 26, but the well-defined main sequence appears to terminate at the hydrogen burning mass limit of $M \sim 0.072\,M_\odot$, or $V \sim 24$, with a few candidate brown dwarfs found below this limit, but with high field contamination.

We also considered using the model isochrones of Baraffe et al. (1998) and Chabrier et al. (2000) for selecting candidate members.
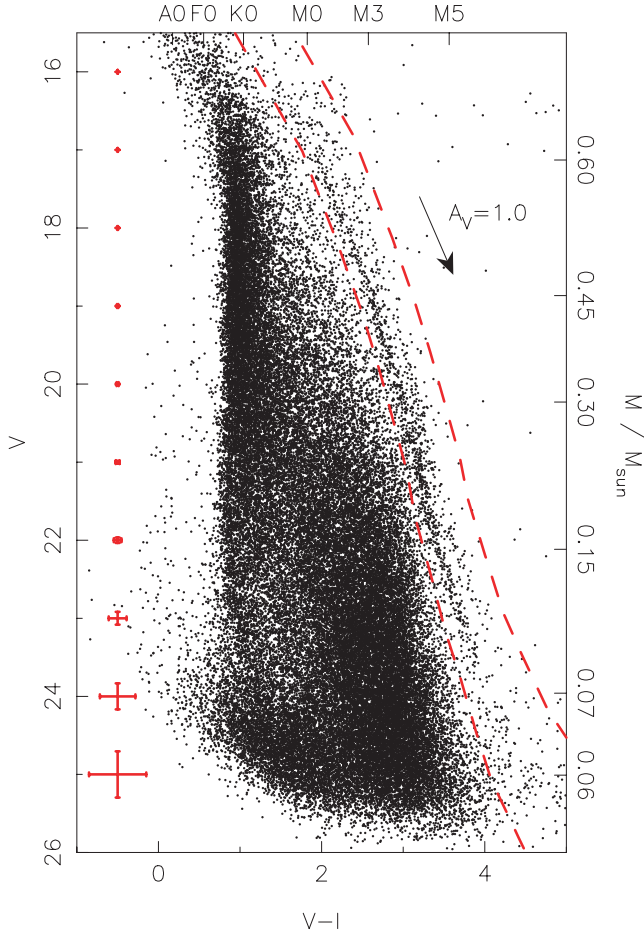
Figure 4. *V* versus *V − I* CMD of NGC 2516 from stacked images, for all objects with stellar morphological classification. The cluster main sequence is clearly visible on the right-hand side of the diagram. The boundaries of the region to select photometric candidate members are shown by the dashed lines (all objects between the dashed lines were selected). The reddening vector for $A_V = 1.0$ is shown at the right-hand side of the diagram. The mass scale is from the 150-Myr NextGen models (Baraffe et al. 1998) for $M > 0.1 \, M_\odot$, and the 120-Myr DUSTY models (Chabrier et al. 2000) for $M < 0.1 \, M_\odot$, using our empirical isochrone to convert the *V* magnitudes to *I* magnitudes, and subsequently obtaining the masses from these, due to known problems with the *V* magnitudes from the models (see Section 3.1). The error bars at the left-hand side of the plot indicate the typical photometric error for an object on the cluster sequence.

The NextGen model isochrones were found to be unsuitable due to the known discrepancy between these models and observations in the $V - I$ colour for $T_{\rm eff} \lesssim 3700 \, {\rm K}$ (corresponding here to $V - I \gtrsim 2$). This was examined in more detail by Baraffe et al. (1998), and is due to a missing source of opacity at these temperatures, leading to overestimation of the *V*-band flux. Consequently, when we have used the NextGen isochrones to determine model masses and radii for our objects, the *I*-band absolute magnitudes were used to perform the relevant look-up, since these are less susceptible to the missing source of opacity, and hence give more robust estimates.

3.2 Completeness

The completeness of our source detection was estimated by inserting simulated stars at random *x, y* positions into our images, drawing the stellar magnitudes from a uniform distribution. Fig. 5 shows the
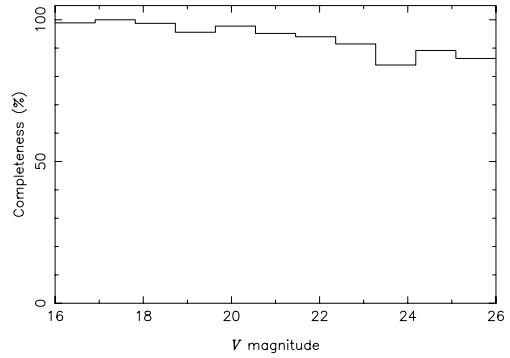

Figure 5. Completeness in our source detection, measured as the fraction of simulated objects which were detected in each magnitude bin. The diagram is plotted in the Johnson *V* system assuming objects to lie on the empirically derived cluster main-sequence track of Section 3.1 and Fig. 4. The diagram has been terminated at $V = 26$ since we have not continued the selection of cluster members past this magnitude due to termination of the apparent main sequence in the CMD of Fig. 4.

resulting plot of completeness as a function of *V*-band magnitude. The completeness for objects on the cluster sequence is >90 per cent down to the brown dwarf limit ($V \sim 24$). We suspect that the gradual drop in completeness toward fainter magnitudes in Fig. 5 results from a variable background in our CCD images caused by haloes and scattered light from the many bright stars in the cluster field, impeding detection of faint sources in certain regions of the frame.

3.3 Contamination

In order to estimate the level of contamination in our catalogue, we used the Besançon Galactic models (Robin et al. 2003) to generate a simulated catalogue of objects passing our selection criteria at the Galactic coordinates of NGC 2516 ($l = 273°.8, b = −15°.9$), covering the total field of view of $\sim 1.1 \, {\rm deg}^2$ (including gaps between detectors). We selected all objects over the apparent magnitude range $14 < V < 26$, giving 105 000 stars. The same selection process as above for the cluster members was then applied to find the contaminant objects. A total of 651 simulated objects passed these membership selection criteria, giving an overall contamination level of ~ 39 per cent. Fig. 6 shows the contamination as a function of *V* magnitude. We note that this figure is somewhat uncertain due to the need to use Galactic models. Follow-up data (spectroscopy) will be required to make a more accurate estimate. We note in particular that the apparently very high contamination in the $V = 16–17$ bin, and possibly also the $V = 25–26$ bin, is probably the result of the model poorly fitting the observations, causing the contamination level to be overestimated.

3.4 Binary fraction

Since the cluster binary sequence is so clearly visible in the CMD of Fig. 4, we have computed a simple photometric lower limit for the binary fraction in the cluster as a function of mass, using the empirical isochrone to select stars with luminosities lying within a band of height $2.5 \log_{10} 2 \simeq 0.75$ mag centred on the single star cluster sequence, and the binary sequence (obtained by shifting the cluster sequence by this amount to greater luminosities), illustrated in Fig. 7. This technique suffers from several sources of systematic error, including (a) since the single star sequence is closer to the
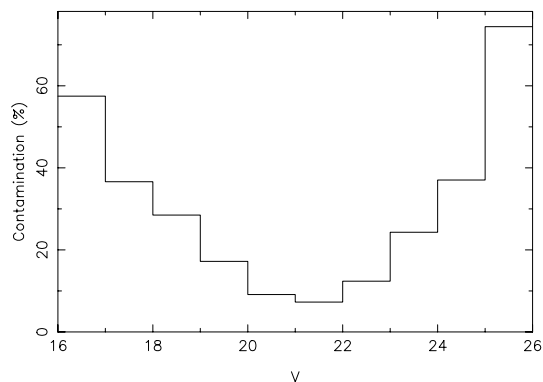
Figure 6. Contamination, measured as the ratio of the calculated number of objects in each magnitude bin from the Galactic models, to the number of objects detected and classified as candidate cluster members in that magnitude bin.
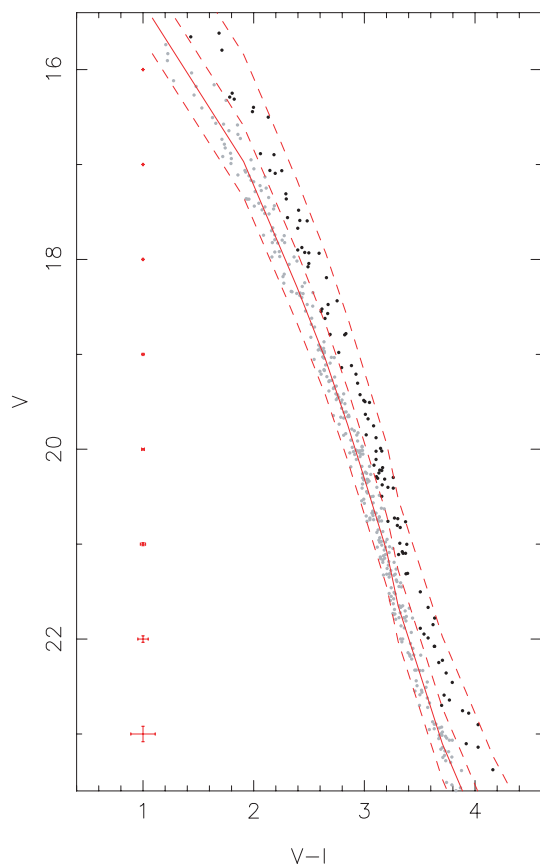

Figure 8. Photometric binary fraction as a function of stellar mass (computed using the NextGen models of Baraffe et al. 1998).

CMD the binaries are brighter, and hence more readily detected than single stars of the same colour.

The binary fraction is shown as a function of mass in Fig. 8. A total of 357 candidate binaries and 1065 candidate single stars were selected, giving an overall binary fraction of 33.5 ± 2.1 per cent (using Poisson errors).

We have been unable to use the more traditional $I - K$ CMD approach (e.g. Pinfield et al. 2003) to determining limits on the binary fraction due to the lack of suitable near-infrared (IR) data. Two Micron All Sky Survey (2MASS) provides K-band photometry, but the resulting $I - K$ CMD did not show a clearly visible binary sequence due to the large scatter caused by the photometric errors at the faint end of 2MASS.

At this point, it is prudent to examine the sensitivity of our selection to the mass ratio q of the binaries. To do this, we have simulated binaries over a range of q from 0 to 1.0, using the pre-main sequence models to compute the total I-band luminosity of the binary, and our empirical isochrone to convert the individual I-band magnitudes of the primary and secondary to V band, and hence place the objects on the $V - I$ CMD. Our selection was then applied to determine the minimum mass ratio q for the detected binaries, defined as $q = M_2/M_1$ (where M_1 and M_2 are the primary and secondary masses, respectively). The results of this procedure are shown in Fig. 9. In general we find that our selection is sensitive to smaller mass ratios at lower masses, which could explain the form of the binary fraction as a function of mass seen in Fig. 8. The figure indicates that we are sensitive to $q \gtrsim 0.7$ over the entire mass range, and at best, $q \gtrsim 0.3$ at $M \sim 0.2 \, M_\odot$. Comparing these values to those of Pinfield et al. (2003), we find that the $V - I$ selection is slightly less sensitive to unequal mass ratio systems (e.g. in their 0.6–1.0 $M_\odot$ bin the minimum detectable mass ratio was $q = 0.5$ whereas here it is $q = 0.6$).

We note that since the completeness in Fig. 5 is close to constant over the entire mass range covered by Fig. 8, the apparent increase in binary fraction toward lower masses is probably not an incompleteness effect resulting from lower completeness for the single star sequence, compared to the more luminous binary sequence. However, our selection is affected by field contamination, with a background of field objects falling inside the selection bins on the CMD. This will tend to decrease the computed binary fraction, since there are more field objects at the single star side of the selection region (see Fig. 4). It is difficult to correct for this effect until we have obtained follow-up spectroscopy.

Our results in $V - I$ are in good general agreement with those of Pinfield et al. (2003), although it is difficult to distinguish whether

Figure 7. V versus $V - I$ CMD, as Fig. 4, showing the selection of photometric candidate single stars (grey) and binaries (black). The solid line shows the original empirical cluster main sequence, and the dashed lines show the boundaries used for selection, with V-band magnitudes $V + 1.25 \log_{10} 2$, $V - 1.25 \log_{10} 2$ and $V - 3.75 \log_{10} 2$, where V is the empirical main-sequence magnitude. Typical photometric errors are indicated as for Fig. 4 by the error bars at the left-hand side of the diagram.

maximum of the distribution of field stars in the CMD, the single star counts are increased to a greater degree than the binary counts by field contamination, (b) binaries with mass ratios significantly different from 1 lie closer to the single star sequence, and therefore tend not to be selected as binaries and (c) at the faint end of the
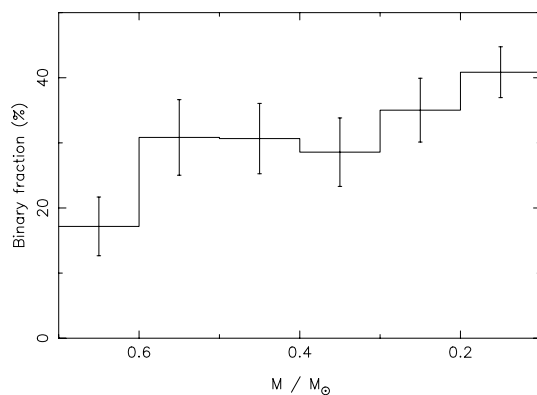
our data are consistent with any change in the binary fraction as a function of mass, given the small number statistics (and hence large Poisson errors in Fig. 8) and better sensitivity to small q with decreasing mass (leading presumably to more detections).

Photometric selection of binaries remains, to our knowledge, relatively untested, without detailed evaluation of the sensitivity. Therefore, a more detailed and reliable study of binarity in NGC 2516 requires follow-up spectroscopy.

4 PERIOD DETECTION

4.1 Method

The method we use for detection of periodic variables is described in detail in Irwin et al. (2006), and we provide only a brief summary here. The method uses least-squares fitting of sine curves to the time-series $m(t)$ (in magnitudes) for *all* candidate cluster members, using the form

$$m(t) = m_{dc} + \alpha \sin(\omega t + \phi), \tag{4}$$

where m_{dc}, α (the amplitude) and ϕ (the phase) are free parameters at each value of ω over an equally spaced grid of frequencies, corresponding to periods from 0.005 to 50 d for the present data set.

Periodic variable light curves were selected by evaluating the change in reduced χ^2:

$$\Delta\chi_\nu^2 = \chi_\nu^2 - \chi_{\nu,\text{smooth}}^2 > 0.4, \tag{5}$$

where χ_ν^2 is the reduced χ^2 of the original light curve with respect to a constant model, and $\chi_{\nu,\text{smooth}}^2$ is the reduced χ^2 of the light curve with the smoothed, phase-folded version subtracted. This threshold was used for the M34 data and appears to work well here too, carefully checked by examining all the light curves for two of the detectors, chosen randomly. A total of 1011 objects were selected by this automated part of the procedure.

The selected light curves were examined by eye to define the final sample of periodic variables. A total of 362 light curves were selected, with the remainder appearing non-variable or too ambiguous to be included.

4.2 Simulations

Monte Carlo simulations were performed following the method detailed in Irwin et al. (2006), injecting simulated signals of 2 per cent amplitude and periods chosen following a uniform distribution on $\log_{10}$ period from 0.1 to 20 d, into light curves covering a uniform distribution in mass, from 0.7 to $0.1\,M_\odot$. A total of 2271 objects were simulated.

The results of the simulations are shown in Fig. 10 as grey-scale diagrams of completeness, reliability and contamination as a function of period and stellar mass. Broadly, our period detections are close to 100 per cent complete down to $0.2\,M_\odot$, with remarkably little period dependence. The slight incompleteness (approximately 63 per cent completeness for $0.6 < M/M_\odot < 0.7$) seen in the highest mass bin is a result of saturation. Fig. 11 shows a comparison of the detected periods with real periods for our simulated objects, indicating remarkably high reliability, especially compared to the earlier M34 data set (Irwin et al. 2006), resulting from better sampling.

4.3 Detection rate and reliability

The locations of our detected periodic variable candidate cluster members on a V versus $V - I$ CMD of NGC 2516 are shown in
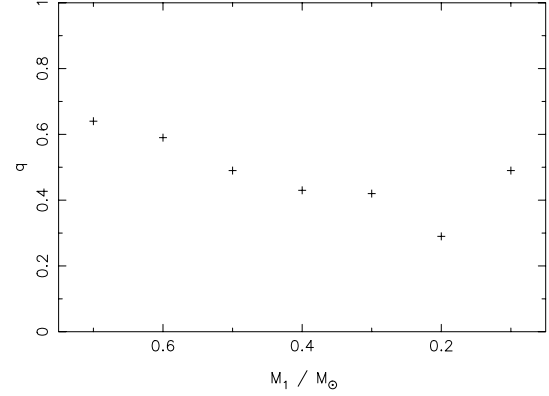

Figure 9. Minimum mass ratio q for detection of binaries as a function of the primary mass M_1 using our CMD approach. Computed using the NextGen (for $M > 0.1\,M_\odot$) and DUSTY (Chabrier et al. 2000) models (for $M \leqslant 0.1\,M_\odot$) to convert between mass and I-band absolute magnitude, and our empirical main-sequence isochrone to convert between I-band and V-band magnitudes. The curve is not smooth owing to the coarse binning used in our empirical isochrone.

Fig. 12. The diagram indicates that the majority of the detections lie on the single-star cluster main sequence, as would be expected for rotation in cluster stars as opposed to, say, eclipsing binaries. The measured photometric binary fraction (see Section 3.4) for the periodic variable stars is 26.3 ± 3.5 per cent (using Poisson errors). This value is slightly lower than the value for all cluster members from Section 3.4, but only at the 1.8σ level. Given the systematic uncertainties in the binary fractions (which are not accounted for by the Poisson counting errors), this is probably not a significant result.

Fig. 13 shows the fraction of cluster members with detected periods as a function of V magnitude. The decaying parts of the histogram at the bright and faint ends may be caused by the increased field contamination here (see Fig. 6), since we expect field objects on average show less rotational modulation than cluster objects, and/or incompleteness effects resulting from saturation for $V \lesssim 17$, and for $V \gtrsim 21$, the gradual increase in the minimum amplitude of variations we can detect (corresponding to the reduction in sensitivity moving to fainter stars, see Fig. 3).

In the M34 survey of Irwin et al. (2006), we commented on a possible increase in the fraction of photometric variables from K to M spectral types, subject to a large uncertainty due to small number statistics. Since the mass range covered by the present sample is different, direct comparison is difficult, and there is no clear evidence for such a trend in NGC 2516. We further note that the decline observed in M34 at faint magnitudes is probably indeed due to incompleteness as stated by Irwin et al. (2006), since a similar trend is also seen in the NGC 2516 data set, displaced accordingly for the differences in sensitivity and distance modulus.

We note that lower field contamination (as evaluated in Section 3.3) is expected in the rotation sample than in the full candidate membership sample. Typical field population ages for the young disc of 3 Gyr (Mayor 1974; Meusinger, Stecklum & Reimann 1991) imply slower rotation rates by factors of a few than cluster members, reduced activity, implying smaller asymmetric components of the spot coverage and hence lower photometric amplitudes (which probably render many of them undetectable).

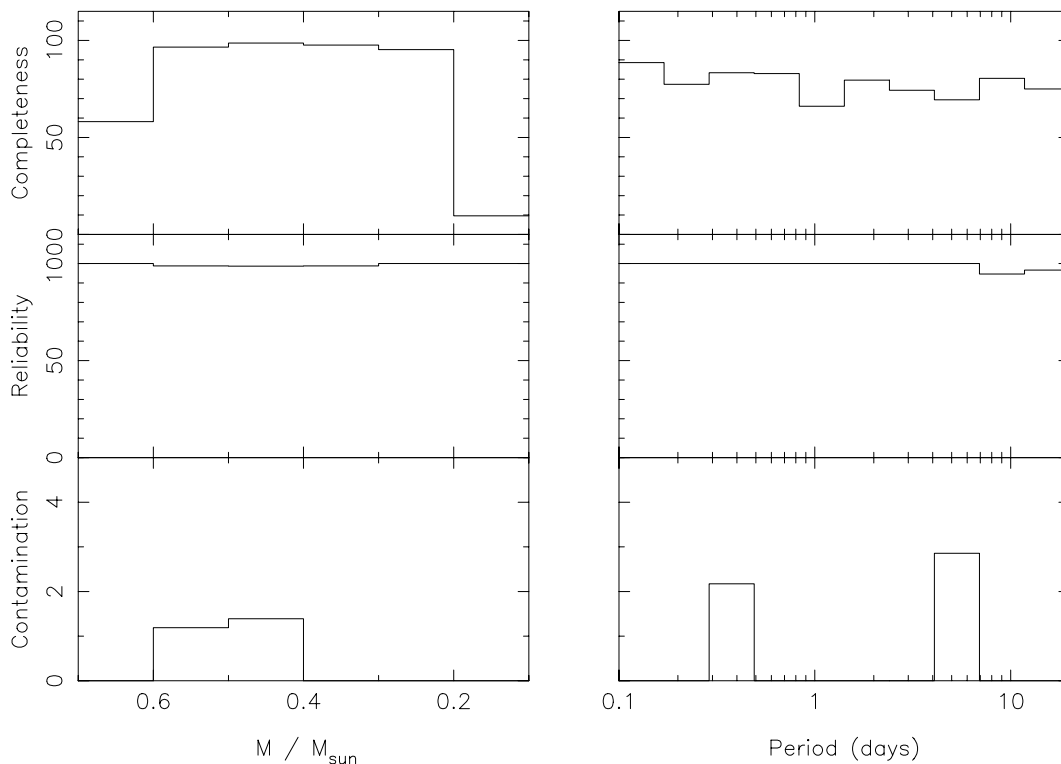The properties of all our rotation candidates are listed in Table 1.

Figure 10. Results of the simulations for 0.02 mag amplitude, plotted as a function of mass (left) and period (right). The simulated region covered $0.1 < M/M_\odot < 0.7$ in order to be consistent with the NGC 2516 sample. Top panels: completeness as a function of real (input) period. Centre panels: reliability of period determination, plotted as the fraction of objects with a given true period, detected with the correct period (defined as differing by <20 per cent from the true period). Bottom panels: contamination, plotted as the fraction of objects with a given detected period, having a true period differing by >20 per cent from the detected value.
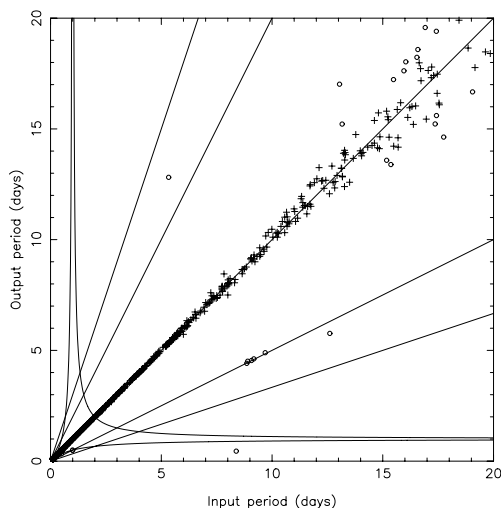

Figure 11. Detected period as a function of actual (input) period for our simulations. Objects plotted with crosses had fractional period error <10 per cent, open circles >10 per cent. The straight lines represent equal input and output periods, and factors of 2, 3, 1/2 and 1/3. The curved lines are the loci of the $\pm 1\,d^{-1}$ aliases resulting from gaps during the day. The majority of the points fall on (or close to) the line of equal periods.

4.4 Non-periodic objects

The population of objects rejected by the period detection procedure described in Section 4 was examined, finding that the most

variable population of these light curves (which might correspond to non-periodic or semiperiodic variability) was contaminated by a small number of light curves ($\sim$50) exhibiting various uncorrected systematic effects, mostly seeing-correlated variations due to image blending. It is therefore difficult to quantify the level of non-periodic or semiperiodic variability in NGC 2516 from our data. Qualitatively, however, there appear to be very few of these variables, and examining the light curves indicated only $\sim$10 obvious cases, some of which resembled eclipses (either planetary transits or eclipsing binaries), and will be the subject of a later Monitor project paper.

5 RESULTS

5.1 NGC 2516 rotation periods

Plots of period as a function of $V - I$ colour and mass for the objects photometrically selected as possible cluster members are shown in Fig. 14. These diagrams show a striking correlation between stellar mass (or spectral type) and the longest rotation period seen at that mass, with a clear lack of slow rotators at very low masses. This trend is also followed by the majority of the rotators, with only a tail of faster rotators to $\sim$0.25-d periods. Furthermore, very few objects were found rotating faster than this, implying a hard lower limit to the observed rotation periods at 0.25 d.

Could the apparent morphology in Fig. 14 be explained by sample biases? The simulations of Section 4.2 suggest that this is unlikely, since we are sensitive to shorter periods than the 0.2–0.3 d 'limit', and the slight bias toward detection of shorter periods at low mass is not sufficient to explain the observations for the slow rotators.
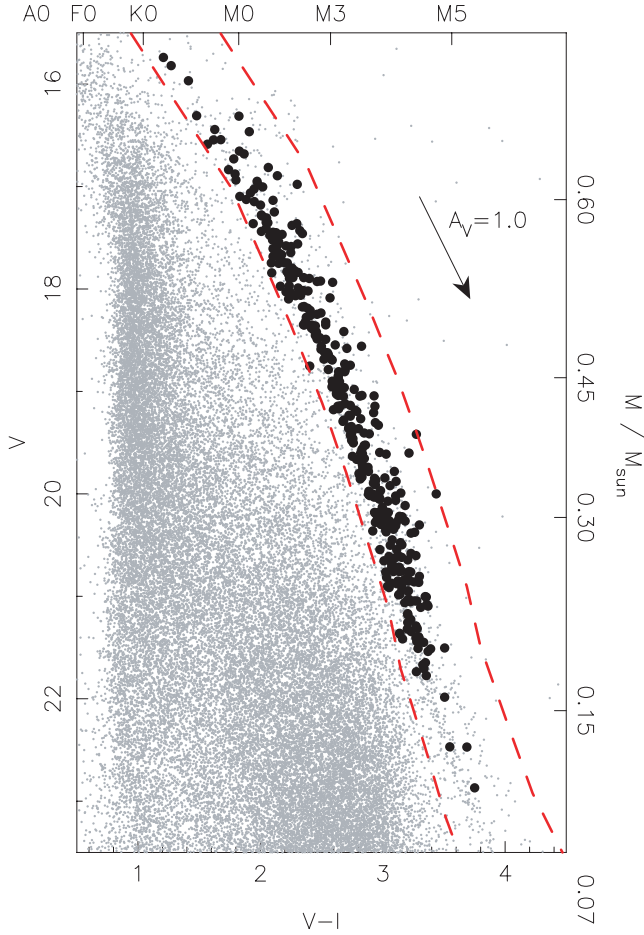
Figure 12. Magnified *V* versus *V − I* CMD of NGC 2516, for objects with stellar morphological classification, as Fig. 4, showing all 362 candidate cluster members with detected periods (black points). The dashed lines show the cuts used to select candidate cluster members (see Section 3.1).

Furthermore, Fig. 15 indicates that the lack of sensitivity to low amplitudes at low masses does not appear to introduce any systematic changes in the detected periods.

Figs 14 and 15 show an apparent lack of objects with masses $0.2 < M/M_\odot < 0.4$ and rotation periods $\gtrsim 2$ d, a region of the diagram where our survey is sensitive down to amplitudes of 0.01 mag (see also Section 4.2). There is also an apparent lack of large-amplitude objects in this region of the diagram, although this is not statistically significant (applying a Kolmogorov–Smirnov test between the two mass bins indicated a probability of 0.25 that the distributions were drawn from the same parent population).

5.1.1 Period distributions

In order to quantify the morphology of Fig. 14, we have used histograms of the rotation period distributions in two broad mass bins, $0.4 \leqslant M/M_\odot < 0.7$ and $M < 0.4\,M_\odot$, shown in Fig. 16. We have attempted to correct the distributions for the effects of incompleteness and (un)reliability using the simulations described in Section 4.2, following the method used in Irwin et al. (2006). The results of doing this are shown in the solid histograms in Fig. 16, and the raw period distributions in the dashed histograms.

The period distributions in the two mass bins of Fig. 16 show clear differences, with the low-mass stars ($M < 0.4\,M_\odot$) showing
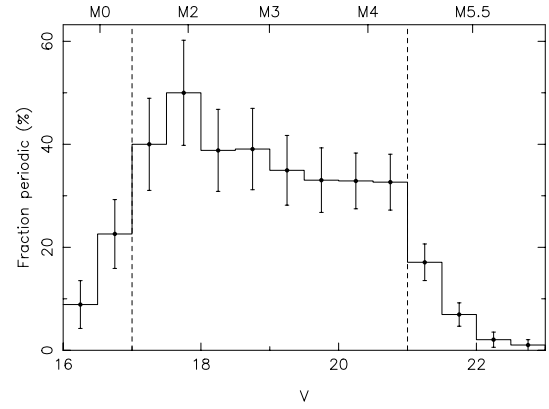

Figure 13. Fraction of candidate cluster members detected as periodic variables, plotted as a function of magnitude. This distribution has not been corrected for incompleteness in the period detections, which are close to 100 per cent complete for $17 < V < 21$ (shown by the vertical dashed lines).

a strongly peaked rotational period distribution, with a maximum at ∼0.6–0.7 d, whereas the higher mass stars ($0.4 \leqslant M/M_\odot < 0.7$) show a broader distribution. We applied a two-sided Kolmogorov–Smirnov test to the corrected distributions to confirm the statistical significance of this result, finding a probability of 4×10^{-20} that the distributions were drawn from the same parent population.

The implication of this result is that the observed morphology in Fig. 14, and in particular the increase of the longest observed rotation period as a function of increasing mass, a trend followed also by the bulk of the rotators, is real and statistically significant.

5.1.2 Low-mass slow rotators

A group of ∼4 outliers are visible e.g. in the upper panel of Fig. 14, as unusually slow rotators at low mass ($(V − I) \gtrsim 2.5$). These objects also give rise to the apparent 'trend' seen in Fig. 15 of smaller amplitudes for periods $P \gtrsim 2$ d, for the lower mass bin ($0.2 < M/M_\odot \leqslant 0.4$).

Careful examination of the light curves indicates that these objects are all convincing detections, and lie on, or close to, the cluster sequence. Obtaining optical spectroscopy for these objects would appear to be warranted, to constrain their membership of the cluster, and determine spectral types, to evaluate their reddening.

5.1.3 Rapid rotators

We have examined the periods of our fastest rotating stars, to check if they are rotating close to their breakup velocity. The critical period $P_{\rm crit}$ for breakup is given approximately by

$$P_{\rm crit} = 0.116\,{\rm d}\,\frac{(R/{\rm R}_\odot)^{3/2}}{(M/{\rm M}_\odot)^{1/2}},\qquad(6)$$

where R and M are the stellar radius and mass, respectively (e.g. Herbst et al. 2002). Using the NextGen models of Baraffe et al. (1998), the object rotating closest to breakup is N2516-2-8-624, with $P_{\rm crit}/P = 0.42$. However, the majority of our objects are rotating at much lower fractions of their break-up velocity.

Fig. 15 indicates that all but three of our fastest rotators have $P > 0.2$ d. The outliers are N2516-1-4-3373 ($P = 0.148$ d), N2516-2-8-566 ($P = 0.146$ d) and N2516-2-8-624 ($P = 0.087$ d). Two of these objects, N2516-1-4-3373 and N2516-2-8-624, clearly lie on

Table 1. Sample of the properties of our 362 rotation candidates. The period *P* in days, *i*-band amplitude α_i (units of magnitudes, in the instrumental bandpass), interpolated mass and radius (from the models of Baraffe et al. 1998, derived using the *I* magnitudes) are given (where available). Our identifiers are formed using a simple scheme of the cluster name, field number, CCD number and a running count of stars in each CCD, concatenated with dashes. The full table is available on Blackwell Synergy as Supplementary Material to the online version of this paper.

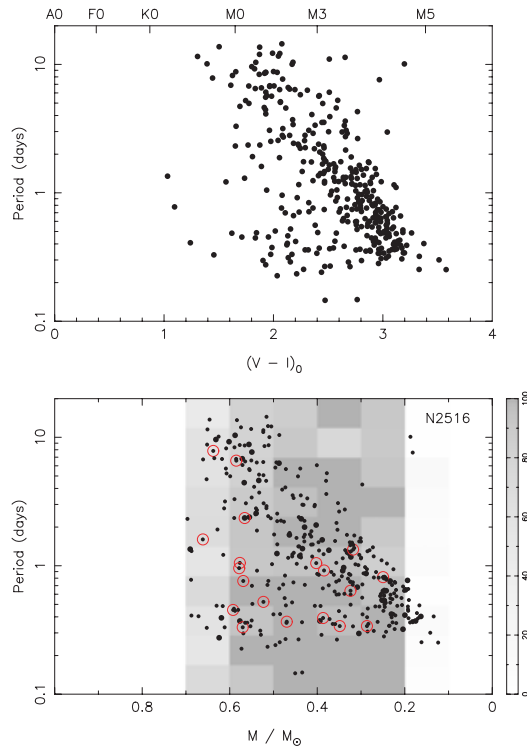| Identifier	RA (J2000)	Dec. (J2000)	*V* (mag)	*I* (mag)	*P* (d)	α_i (mag)	*M* (M$_\odot$)	*R* (R$_\odot$)
N2516-1-1-351	07^{h}56^{m}28^{s}22	−61°27′46″6	18.99	16.35	2.318	0.016	0.44	0.41
N2516-1-1-784	07^{h}56^{m}43^{s}99	−61°30′51″5	21.25	18.05	0.649	0.013	0.20	0.24
N2516-1-1-881	07^{h}56^{m}47^{s}57	−61°34′37″9	17.80	15.54	7.677	0.010	0.55	0.51
N2516-1-1-958	07^{h}56^{m}49^{s}99	−61°32′19″9	18.48	15.99	6.291	0.015	0.49	0.45
N2516-1-1-1470	07^{h}57^{m}08^{s}92	−61°29′18″6	17.67	15.49	8.803	0.016	0.56	0.52

Figure 14. Plots of rotation period as a function of dereddened $V - I$ colour (top), and mass (bottom) for NGC 2516, deriving the masses using the 150 Myr NextGen mass–magnitude relations of Baraffe et al. (1998) and our measured *I*-band magnitudes. In the lower diagram, the grey-scales show the completeness for 0.02 mag periodic variations from our simulations, and X-ray sources from Pillitteri et al. (2006) are overlaid with open circles.

Figure 15. Plot of amplitude as a function of period for NGC 2516 in two mass bins: $0.4 < M/\mathrm{M}_\odot < 0.7$ (top) and $0.2 < M/\mathrm{M}_\odot < 0.4$ (bottom).

the binary sequence in Fig. 4, and N2516-2-8-566 may also lie on the binary sequence, so we suspect that these stars might be tidally locked binaries. They are therefore good candidates for spectroscopic follow-up.

We note that there are three outliers visible in Fig. 14 with $(V - I)_0 \lesssim 1.3$, and periods close to 1 d. Similar objects were seen in our M34 study (Irwin et al. 2006). At these masses, field contamination in our survey is significant (∼60 per cent), so we suspect that they may be contaminating field objects, and possibly binaries (in M34, several of the corresponding objects were also detected in X-rays, it is difficult to say if this holds in NGC 2516 due to the incomplete overlap in spatial coverage with the X-ray catalogue of Pillitteri et al. 2006). Our survey is incomplete at these (high) masses due
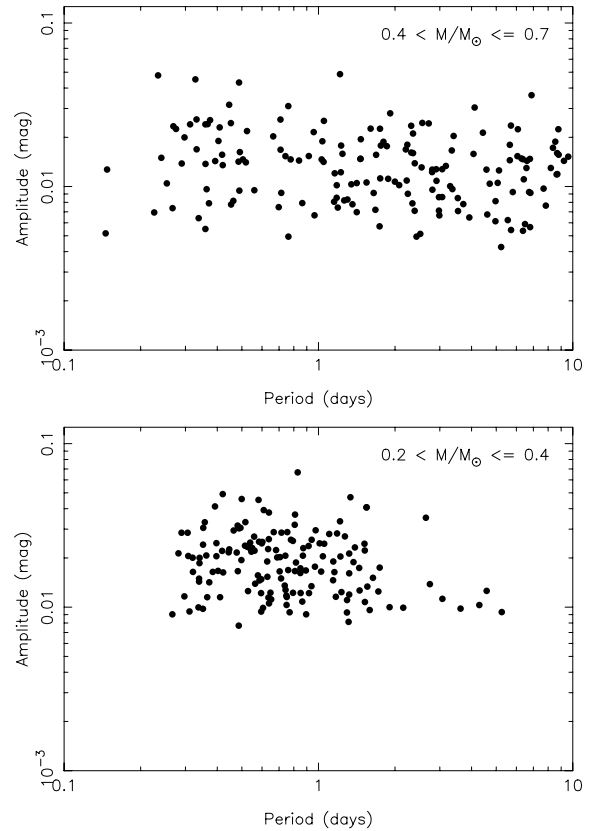
to saturation of the detectors, which varied between CCDs in the mosaic, giving rise to the lack of other objects detected in this range of $(V - I)_0$.

5.2 Comparison with other data sets

5.2.1 Period versus mass diagram

Fig. 17 shows a diagram of rotation period as a function of stellar mass for the Orion Nebula cluster (ONC) (1 ± 1 Myr; Hillenbrand 1997), NGC 2264 (2–4 Myr; Park et al. 2000), NGC 2362 (∼5 ± 1 Myr; Balona & Laney 1996; Moitinho et al. 2001), the Pleiades (∼100 Myr; Meynet et al. 1993), NGC 2516 and M34 (∼200 Myr; Jones & Prosser 1996). Data sources for each cluster are indicated
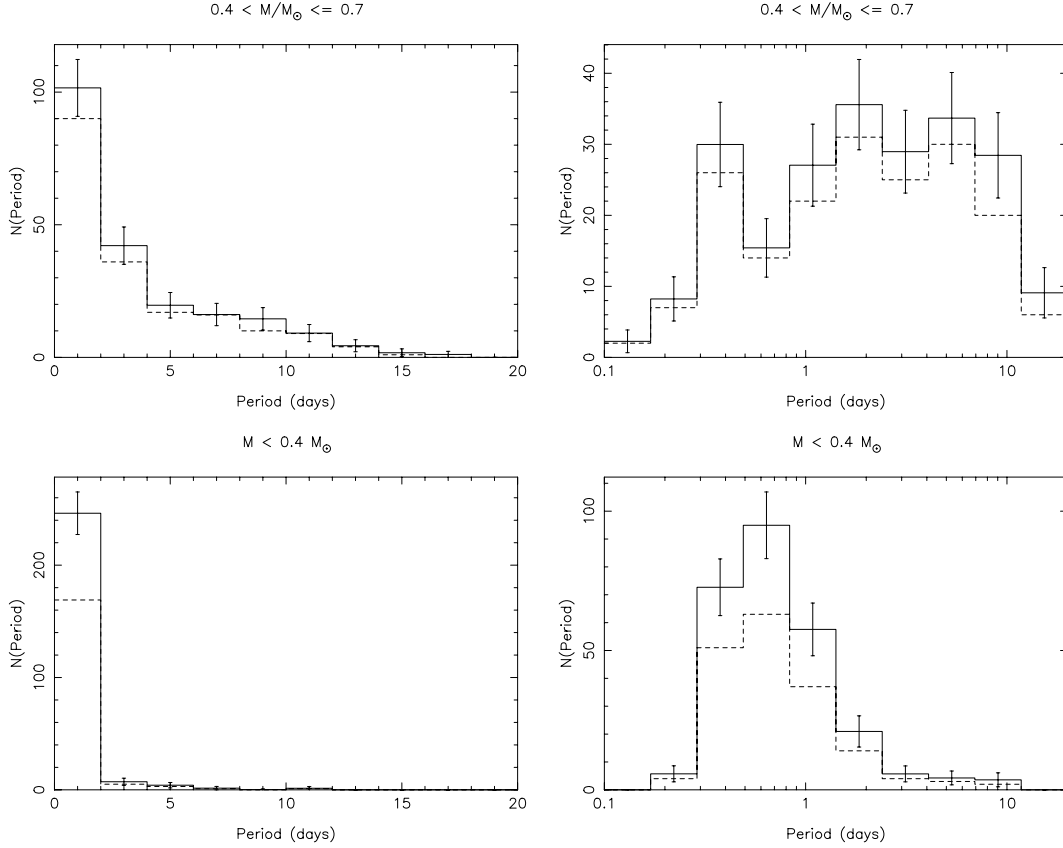
Figure 16. Period distributions for objects classified as possible photometric members, in two mass bins: $0.4 \leqslant M/M_\odot < 0.7$ (upper row, corresponding roughly to early-M spectral types) and $M < 0.4\,M_\odot$ (lower row, late M). The left-hand panels show the distributions plotted in linear period, and the right-hand panels show the same distributions plotted in $\log_{10}$ period. The dashed lines show the measured period distributions, and the solid lines show the results of attempting to correct for incompleteness and reliability, as described in the text.

in the figure caption. From this figure, it appears that the objects we observe in NGC 2516 are bounded by lines of $P \sim$ constant (or a low power of M) for the fastest rotators, and $P \propto M^3$ for the slow rotators in the mass range $0.2 < M/M_\odot < 0.7$.

Furthermore, comparing the NGC 2516 and M34 results in Fig. 17 indicates that the slowest rotators for $M > 0.6\,M_\odot$ have $P \sim$ constant as a function of mass, whereas for $M < 0.6\,M_\odot$, the period increases as a function of mass. A similar trend is visible in the Pleiades $v \sin i$ data (noting that a number of the slowest rotators here only have $v \sin i$ lower limits, denoted by double-headed arrows).

The diagram clearly shows a gradual evolutionary sequence, from a relatively flat mass dependence of the rotation periods in the ONC ($\sim$1 Myr) to a sloping relation in NGC 2362 ($\sim$5 Myr), and the emergence of the break between a flat distribution for $M \gtrsim 0.6\,M_\odot$ and strongly sloping distribution at lower masses, for the Pleiades, NGC 2516 ($\sim$150 Myr) and M34 ($\sim$200 Myr). We suggest this apparent change in slope at $M \sim 0.6\,M_\odot$ may correspond to a transition to convectively dominated stellar interiors moving to lower masses (but see Section 6.2).

5.2.2 *v sin i measurements*

Terndrup et al. (2002) presented $v \sin i$ measurements for G and early-K dwarfs in NGC 2516. Dividing their sample into branches of fast and slow rotation for $(B - V)_0 > 0.6$ and counting objects with $v \sin i < 15\,\mathrm{km\,s}^{-1}$ as slow rotators, gave seven fast rotators, with typical $v \sin i \sim 20$–$50\,\mathrm{km\,s}^{-1}$, and 17 slow rotators with

$v \sin i \lesssim 10\,\mathrm{km\,s}^{-1}$, i.e. 30 per cent are fast rotators. The threshold of $v \sin i = 15\,\mathrm{km\,s}^{-1}$ corresponds to $P = 2.2 \sin i$ d at $0.7\,M_\odot$, or $\langle P \rangle = 1.72$ d, using $\langle \sin i \rangle = \pi/4$ (averaged over all inclinations i). Applying this threshold to the 0.5–$0.7\,M_\odot$ bin of Fig. 14, we counted 69 slow rotators and 40 fast rotators, i.e. 37 per cent fast rotators (and clearly from Fig. 14 this fraction increases considerably for lower masses, to nearly 100 per cent at $0.2\,M_\odot$). Furthermore, for $(B - V)_0 < 0.6$ there are no clearly visible fast rotators in fig. 5 of Terndrup et al. (2002). These results clearly indicate that the fraction of objects rotating faster than the chosen threshold increases as a function of mass, lending support to the rotation period results we have presented.

5.2.3 *Comparison to the field: main-sequence spin-down*

Comparing our results with the field survey of Delfosse et al. (1998) indicates that the spin-down time-scale of M dwarfs increases moving to later spectral types (or lower masses). The fastest rotators observed by these authors in the young disc population (age $\sim$3 Gyr; Mayor 1974; Meusinger et al. 1991) were of $\sim$M4 spectral type, with $P/\sin i \sim 12$ h. Given that we expect the objects to spin-down on the main sequence, their origin must be in the most rapid rotators of the present sample ($\sim$0.25 d), suggesting a factor of only $\sim$2 spin-down. This is slower than the Skumanich (1972) $t^{1/2}$ prediction of a factor of $\sim$4.5, suggestive of a very long spin-down time-scale for these late-type dwarfs compared to solar-type dwarfs.
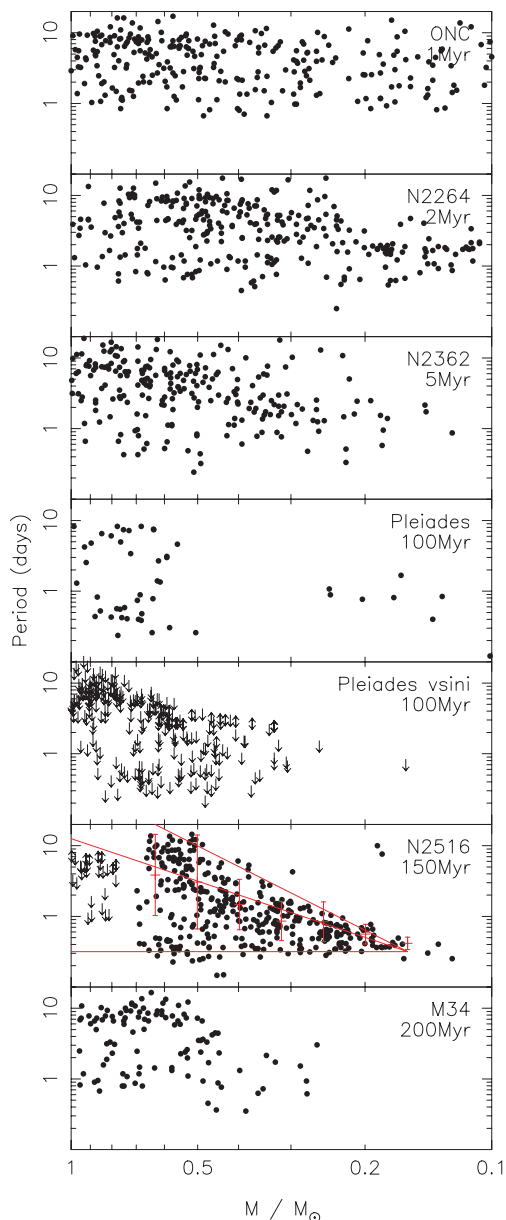
Figure 17. Rotation period as a function of stellar mass for (top to bottom): ONC, NGC 2264, NGC 2362, the Pleiades (rotation periods and $v \sin i$ data on separate plots), NGC 2516 and M34. Lower and upper limits (from $v \sin i$ data) are marked with arrows. The masses were taken from the NextGen mass–magnitude relations (Baraffe et al. 1998) at the appropriate ages. The ONC data are from Herbst et al. (2002). For NGC 2264 we used the data of Makidon et al. (2004) and Lamm et al. (2005). The NGC 2362 data are from the Monitor project, to be published in Hodgkin et al. (in preparation). The Pleiades rotation period data are a compilation of the results from Magnitskii (1987), Stauffer et al. (1987), Van Leeuwen, Alphenaar & Meys (1987), Prosser et al. (1993a,b, 1995), Krishnamurthi et al. (1998) (taken from the open cluster data base), Terndrup et al. (1999) and Scholz & Eislöffel (2004b). The Pleiades $v \sin i$ data are a compilation of results from Stauffer et al. (1984), Stauffer & Hartmann (1987), Soderblom et al. (1993), Jones, Fischer & Stauffer (1996), Queloz et al. (1998) and Terndrup et al. (2000). The M34 data are taken from Irwin et al. (2006). In the NGC 2516 plot, the lines show $P = $ constant, $P \propto M^2$ and $P \propto M^3$. The error bars show the median of the distribution binned in 0.1-dex bins of $\log M$.
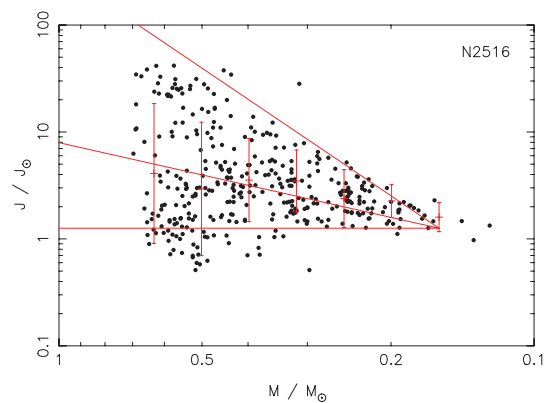

Figure 18. Stellar angular momentum J as a function of mass for the NGC 2516 rotation period sample. The lines show $J = $ constant, $J \propto M$ and $J \propto M^3$. The error bars show the median of the distribution binned in 0.1-dex bins of $\log M$.

6 DISCUSSION

6.1 Link to angular momentum

It is instructive to examine the implications of the relations determined in Section 5.2.1 for the stellar angular momentum J. We define

$$J = I\omega \qquad (7)$$

$$= \frac{2\pi k^2 M R^2}{P}, \qquad (8)$$

where $I = k^2 M R^2$ is the moment of inertia of a star of mass M and radius R, k is the radius of gyration (e.g. $k^2 = 2/5$ for a sphere of uniform density) and $\omega = 2\pi/P$ is the rotational angular velocity.

For a fully convective star ($M \lesssim 0.4\,\mathrm{M_{\odot}}$), k is approximately independent of mass, and therefore the specific angular momentum $j = J/M \propto R^2/P$. Furthermore, on the ZAMS we can approximate $M \propto R$ at these masses.[1] Thus, recalling the simple description of the morphology of the period versus mass plots in terms of power-law relations from Section 5.2.1 and Fig. 17, $P = $ constant implies $j \propto M^2$, and $P \propto M^3$ implies $j \propto M^{-1}$. These correspond to $J \propto M^3$ and $J = $ constant, respectively. A plot of J as a function of stellar mass for the NGC 2516 sample is shown in Fig. 18, with these lines overlaid.

We computed the median rotation period as a function of mass for the NGC 2516 data, finding it was consistent with $P_{\mathrm{med}} \propto M^2$, a relation in between those of the upper and lower envelopes in Fig. 17. This implies $j = $ constant as a function of mass, a result consistent with the conclusions of Herbst, Bailer-Jones & Mundt (2001) in the ONC. The lack of any change in the median relation for stars still undergoing contraction on the PMS indicates that any mass-dependent angular momentum losses are not important in determining the evolution of the median over this age range. However, this is not the case in detail or once the stars reach the ZAMS, in particular the *shape* of the distribution even in this mass range does evolve in a mass-dependent fashion.

---

[1] Fitting the mass–radius relation from the models of Baraffe et al. (1998) over the range $0.1 < M/\mathrm{M_{\odot}} < 0.7$ with a simple linear model gave $R/\mathrm{R_{\odot}} = 0.8\,M/\mathrm{M_{\odot}} + 0.075$, which is a better approximation than the simple proportionality.

It is interesting to compare the present observations with the Pleiades survey of Scholz & Eislöffel (2004b). The mass dependence of the angular momentum evolution we have derived for NGC 2516 appears to be slightly inconsistent with their conclusions, where they found $P \propto M$. Examining the Pleiades diagram in Fig. 17 indicates that their result can most likely be attributed to the lack of data for $0.25 < M/M_\odot < 0.5$. Otherwise the results of the surveys are in good agreement, as expected due to the similar ages of the two clusters.

The earlier conclusions of Scholz & Eislöffel (2004a) in σ Ori (age ~ 3 Myr) are interesting, since they also found $P \propto M$. At these ages, the mass–radius relation is better fit by $R/R_\odot \propto \left(M/M_\odot\right)^{1/2}$, so this implies $P \propto R^2$, or constant specific angular momentum, the same as our median relation.

6.2 Simple models

6.2.1 Description

We have developed a simple model scheme, to attempt to find an explanation for the observations, following the approach of Bouvier et al. (1997) and Allain (1998). In this work, the relation between M, R and k as a function of time for the radiative core (where present) and convective envelope was taken from the Lyon group stellar models, generously supplied to us by I. Baraffe (private communication) for 0.1, 0.2, 0.3, 0.4, 0.6, 0.8 and $1.0\,M_\odot$. We have interpolated the values where necessary for intermediate masses.

The overall angular momentum loss rate was split into two components: losses due to stellar winds, assuming a loss law with saturation at a critical angular velocity ω_{sat} (allowed to vary as a function of mass), and losses due to disc locking, which to a good approximation maintains a constant angular velocity until the circumstellar disc dissipates.

We assume an angular momentum loss law for stellar winds of the form suggested by Kawaler (1988), modified to include saturation of the angular momentum losses above a critical angular velocity ω_{sat}. Barnes & Sofia (1996) argue that saturation at high velocity is required to account for fast rotators on the ZAMS, and may be physically motivated by saturation of the magnetic dynamo activity giving rise to the angular momentum losses. This is supported by observations of several diagnostics of magnetic activity, including saturation of chromospheric emission (e.g. Vilhu 1984).

The adopted angular momentum loss law has the following form:

$$\left(\frac{\mathrm{d}J}{\mathrm{d}t}\right)_{\text{wind}} = \begin{cases} -K\,\omega^3 \left(\frac{R}{R_\odot}\right)^{1/2} \left(\frac{M}{M_\odot}\right)^{-1/2}, & \omega < \omega_{\text{sat}}, \\ -K\,\omega\,\omega_{\text{sat}}^2 \left(\frac{R}{R_\odot}\right)^{1/2} \left(\frac{M}{M_\odot}\right)^{-1/2}, & \omega \geqslant \omega_{\text{sat}}, \end{cases} \quad (9)$$

where ω is the angular velocity of the star, R is its radius and M its mass. K is a constant, chosen to give the correct value of the solar angular momentum for a $1\,M_\odot$ star at the age of the Sun. The value $K = 2.7 \times 10^{47}\,\text{g}\,\text{cm}^2\,\text{s}$ was determined by Bouvier et al. (1997) to satisfy this requirement, with $\omega_{\text{sat}} = 14\,\omega_\odot$. This particular form of angular momentum loss law is found to reproduce the time dependence of rotation between the Hyades age (625 Myr) and the Sun (4.57 Gyr).

The value of ω_{sat} is found to depend on stellar mass (e.g. Barnes & Sofia 1996; Krishnamurthi et al. 1997), and is typically assumed to be inversely proportional to the convective overturn time-scale τ:

$$\omega_{\text{sat}} = \omega_{\text{sat},\odot}\,\frac{\tau_\odot}{\tau}, \quad (10)$$

where the quantities subscripted $\odot$ are those for the Sun (Krishnamurthi et al. 1997). The values of τ were taken from the 200 Myr model of Kim & Demarque (1996) for $M > 0.5\,M_\odot$. Sills, Pinsonneault & Terndrup (2000) found that simply linearly extrapolating these models to lower masses did not work well, and derived a set of empirical values to fit the distribution seen in the Hyades at these masses. We have also found this to be the case for the NGC 2516 data, and adopt the values of Sills et al. (2000), which give a much better fit to the data.

We consider two classes of models: solid body rotation, where the star is considered to rotate as a single solid body, implying that the core and envelope must have the same angular velocity, and differential rotation, where the core and envelope are allowed to decouple, with angular momentum losses from the envelope, and angular momentum transfer on a time-scale τ_{c} between the core and envelope.

In order to account for disc locking, we introduce a disc locking time τ_{disc}, such that for $t < \tau_{\text{disc}}$, the star is locked to the circumstellar disc, and maintains a constant angular velocity in the convective envelope, equal to the initial value. For $t > \tau_{\text{disc}}$, the angular velocity evolves as follows.

For solid body rotation, we can simply differentiate the expression $J = I\,\omega$, where I, J and ω are the quantities for the entire star, with respect to time. The only angular momentum loss is due to stellar winds, so

$$\frac{\mathrm{d}\omega}{\mathrm{d}t} = \frac{\omega}{J} \left(\frac{\mathrm{d}J}{\mathrm{d}t}\right)_{\text{wind}} - \frac{\omega}{I}\frac{\mathrm{d}I}{\mathrm{d}t}. \quad (11)$$

For differential rotation, the core and envelope must be considered separately. For the envelope, two extra terms are added (see Allain 1998, for a full derivation), describing the coupling of angular momentum from the core (first term), and the loss of mass to the core as the star evolves (second term):

$$\frac{\mathrm{d}\omega_{\text{conv}}}{\mathrm{d}t} = \frac{1}{I_{\text{conv}}}\frac{\Delta J}{\tau_{\text{c}}} - \frac{2}{3}\frac{R_{\text{rad}}^2}{I_{\text{conv}}}\omega_{\text{conv}}\frac{\mathrm{d}M_{\text{rad}}}{\mathrm{d}t}$$
$$-\frac{\omega_{\text{conv}}}{J_{\text{conv}}}\left(\frac{\mathrm{d}J_{\text{conv}}}{\mathrm{d}t}\right)_{\text{wind}} - \frac{\omega_{\text{conv}}}{I_{\text{conv}}}\frac{\mathrm{d}I_{\text{conv}}}{\mathrm{d}t},$$

where we assume

$$\Delta J = \frac{I_{\text{conv}}J_{\text{rad}} - I_{\text{rad}}J_{\text{conv}}}{I_{\text{rad}} + I_{\text{conv}}} \quad (12)$$

as suggested by MacGregor (1991).

The corresponding equation for the evolution of the core angular velocity is

$$\frac{\mathrm{d}\omega_{\text{rad}}}{\mathrm{d}t} = -\frac{1}{I_{\text{rad}}}\frac{\Delta J}{\tau_{\text{c}}} + \frac{2}{3}\frac{R_{\text{rad}}^2}{I_{\text{rad}}}\omega_{\text{conv}}\frac{\mathrm{d}M_{\text{rad}}}{\mathrm{d}t} - \frac{\omega_{\text{rad}}}{I_{\text{rad}}}\frac{\mathrm{d}I_{\text{rad}}}{\mathrm{d}t}, \quad (13)$$

where the first two terms again represent coupling of angular momentum to the envelope and mass gained by the core (from the convective envelope), respectively. The final term accounts for the change in moment of inertia of the core as the star evolves.

6.2.2 Evolution from NGC 2362

We first attempt to evolve the observed rotation rates from our survey in NGC 2362 (Hodgkin et al., in preparation) forward in time to reproduce the available rotation period data in NGC 2516. In order to do this, we consider the slowest rotators, characterized by the 25 percentile (the lower quartile) of the distribution of observed angular velocities, ω, and the fastest rotators, characterized by the 90 percentile of the distribution. The discrepancy in measures here
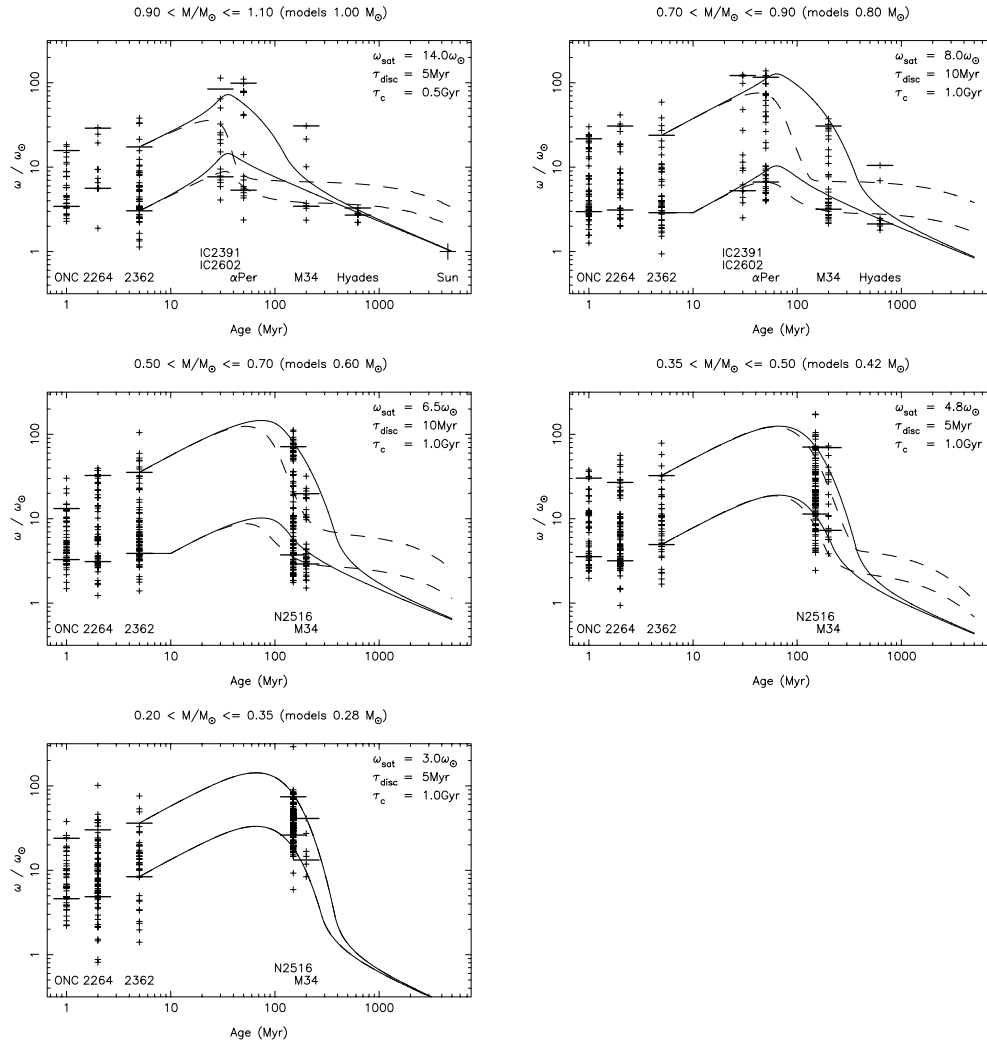
Figure 19. Rotational angular velocity ω plotted as a function of time in five mass bins: $0.9 < M/M_\odot \leqslant 1.1, 0.7 < M/M_\odot \leqslant 0.9, 0.5 < M/M_\odot \leqslant 0.7$, $0.35 < M/M_\odot \leqslant 0.5$ and $0.2 < M/M_\odot \leqslant 0.35$. Crosses show the rotation period data, and short horizontal lines the 25 and 90 percentiles of ω, used to characterize the slow and fast rotators, respectively. The lines show our models for 1.0, 0.8, 0.6, 0.42 and 0.28 $M_\odot$ (respectively), where the solid lines are solid body models, and dashed lines are differentially rotating models, with the parameters shown. Plotted are the ONC (1 Myr), NGC 2264 (2 Myr), NGC 2362 (5 Myr), IC 2391, IC 2602 ($\sim$30 Myr), α Per ($\sim$50 Myr), NGC 2516, M34, the Hyades (625 Myr) and the Sun ($\sim$4.57 Gyr). The IC 2391 data were taken from Patten & Simon (1996) and IC 2602 from Barnes et al. (1999). The α Per data are a compilation of the results from Stauffer et al. (1985), Stauffer, Hartmann & Jones (1989), Prosser (1991), Prosser et al. (1993a,b, 1995), O'Dell & Collier Cameron (1993), O'Dell, Hendry & Collier Cameron (1994), O'Dell at al. (1996), Allain et al. (1996), Martín & Zapatero Osorio (1997), Prosser & Randich (1998), Prosser, Randich & Simon (1998) and Barnes et al. (1998), and the Hyades data from Radick et al. (1987) and Prosser et al. (1995), taken from the open cluster data base.

is because the 10 percentile was found to be somewhat unstable in the presence of small number statistics for slow rotators in some of the clusters under consideration. Nevertheless, the results for this quantity are compatible with the conclusions we draw for the 25 percentile for those clusters with sufficiently good statistics.

We fit solid body and differentially rotating models to the data, allowing the parameters ω_{sat}, τ_{disc} and τ_c to vary to fit the slowest rotators (25 percentile).

Fig. 19 shows our results, where we performed the analysis in a series of mass bins, in order to resolve the mass dependence of the evolution. These were $0.9 < M/M_\odot \leqslant 1.1, 0.7 < M/M_\odot \leqslant 0.9, 0.5 < M/M_\odot \leqslant 0.7, 0.35 < M/M_\odot \leqslant 0.5$ and $0.2 < M/M_\odot \leqslant 0.35$ (chosen empirically to encompass the changes in behaviour seen in the models, while retaining reasonable statistics). The models were calculated for single masses roughly at the centre of these bins of 1.0, 0.8, 0.6, 0.42 and 0.28 $M_\odot$.

The solid body models shown in Fig. 19 show good overall agreement with the upper 90 percentiles for the NGC 2516 data, in all the mass bins. For the $0.9 < M/M_\odot < 1.1$ bin, the M34 upper 90 percentile is at much greater ω than the model, but we suspect that this result is not significant due to small number statistics in the M34 sample at these masses: the discrepancy is due to the presence of three data points, and as discussed in Irwin et al. (2006), these may be contaminants. For $0.7 < M/M_\odot < 0.9$, the upper 90 percentile in the Hyades appears to lie at much greater ω than the model, but again this result is strongly affected by small number statistics. In order to resolve these issues, improved statistics at these masses and ages will be required. We note that the differentially rotating models with the assumed values of τ_c give a poor fit to the fast rotators (as characterized by the 90 percentiles), especially on the ZAMS.

For the lower 25 percentiles, the solid body models give a poor fit to the evolution from NGC 2362 to older ages, which becomes

particularly apparent after ~50 Myr to the age of the Hyades in the top two mass bins. Introducing core–envelope decoupling with $\tau_c = 1.0$ Gyr provides a much better fit to the observations, and produces curves in good agreement with all the presently available data. We note however that we have not constrained these to fit the Sun, which requires a modification of the constant K in equation (9).

An interesting implication of the results in Fig. 19 is that we cannot find a model in this scheme that fits both the slow and fast rotators simultaneously: the values of τ_c required in the models are different (solid body models correspond to $\tau_c = 0$). The result that the fast rotators seem to behave more like solid bodies may indicate that the redistribution of angular momentum at the core/envelope boundary is more efficient in fast rotators.

We note that there are relatively few constraints on the evolution for masses $<0.7\,\mathrm{M_\odot}$ at the intermediate ages (5 to 150 Myr), and at old ages (>200 Myr). We have recently obtained data in NGC 2547 (~38.5 Myr; Naylor & Jeffries 2006) at these masses, which should allow us to address the first of these problems in a forthcoming publication.

6.2.3 Constraints on initial conditions

We explore here an alternative method for analysis of the NGC 2516 data, following Sills et al. (2000). By assuming that all stars share the same initial rotation rate, here 10 d, as used by Sills et al. (2000), we can constrain the disc lifetimes required to reproduce the observed envelope in diagrams of ω as a function of stellar mass. In particular, the observed lower envelope as a function of mass (the slowest rotators seen) must result from the longest disc lifetimes, and hence we can derive the required maximum disc lifetime as a function of mass. Fig. 20 shows the results of this analysis for NGC 2516.

The results in Fig. 20 indicate that the disc lifetime must decrease strongly as a function of decreasing mass in order to reproduce the NGC 2516 data with a single initial rotation period. Lifetimes of >10 Myr are required for $M > 0.3\,\mathrm{M_\odot}$, a result at odds with other measurements (e.g. Haisch, Lada & Lada 2001; Bouwman et al. 2006 and references therein), which indicate values of ~10 Myr at solar mass. Therefore, it seems unlikely that the envelope shape we observe is due purely to varying disc lifetimes as a function of mass.

An alternative explanation (the other extreme) is that the initial period P_0 varies as a function of mass, but the disc lifetime t_{disc} remains fixed. Fig. 21 shows the results of doing this for the NGC 2516 data, assuming $t_{\mathrm{disc}} = 10$ Myr, indicating again that a rather wide range of initial conditions appear to be required to explain the observed envelope purely by variations of P_0. Furthermore, the very slow rotation ($P_0 \sim 60$ d) apparently required at $0.5\,\mathrm{M_\odot}$ is somewhat implausible in light of measurements of very young populations, where typical rotation periods for stars of this mass are ~10 d.

In reality, a combination of the two effects is likely, which will lead to intermediate values of t_{disc} and P_0. However, the required parameter ranges remain implausible in light of existing data. It is possible that improved modelling of the star using a more complete treatment of differential rotation (e.g. Sills et al. 2000) will solve this issue.

6.2.4 Value of ω_{sat}

The value of ω_{sat} at each mass is tightly constrained by the need to reproduce the NGC 2516, M34 and Hyades data. In Section 6.2.2, we derived values for ω_{sat} in coarse mass bins to produce model curves providing a reasonable explanation for the observations. In
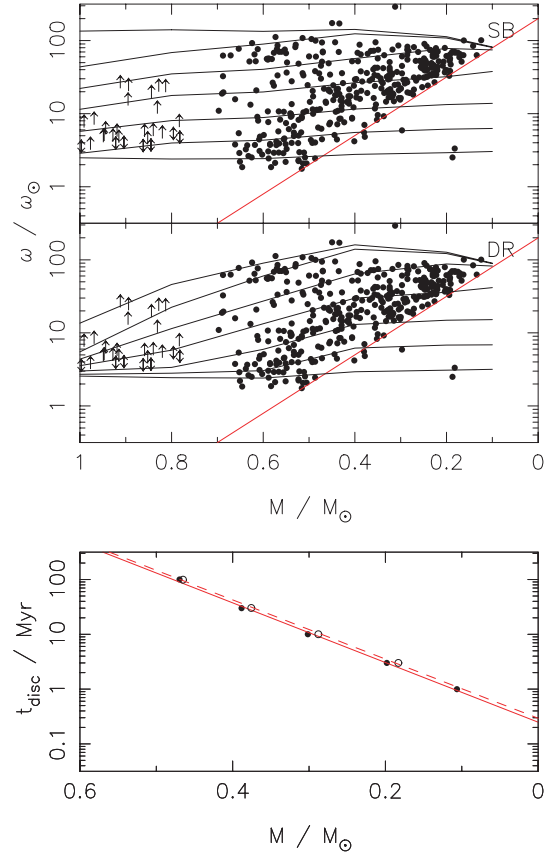

Figure 20. Top and centre: NGC 2516 data (points), plus lower limits derived from the $v \sin i$ values of Terndrup et al. (2002) (arrows), with models overlaid (top: solid body model; centre: differentially rotating model) for $t_{\mathrm{disc}} = 0, 0.3, 1, 3, 10, 30$ and 100 Myr (top to bottom). The initial period P_0 was 10 d. The straight line shows the approximate lower envelope used to derive the disc lifetime as a function of mass. Bottom: derived disc lifetime t_{disc} as a function of mass, for the solid body models (filled circles and solid line), and differentially rotating models (open circles and dashed line). The models used the ω_{sat} values of Sills et al. (2000) (these were adjusted to provide a good fit to the Hyades data).

order to investigate the mass dependence of this parameter in detail, we used the NGC 2362 and 2516 observations to perform a fit of ω_{sat} as a function of mass in much smaller bins to give better sampling, using the same percentile-based technique. Fig. 22 shows the results, finding a linear dependence of ω_{sat} on mass to be a good approximation at the lowest masses, for both solid body and differentially rotating models. There is some evidence that the relation does not apply for higher masses ($M \gtrsim 0.5\,\mathrm{M_\odot}$), but in reality ω_{sat} is not well constrained here, since the majority of these stars (which are slow rotators) only reach the saturation velocity for a short time during the evolution from 5 to 150 Myr.

From the fit, at solar mass, 0.8 and $0.5\,\mathrm{M_\odot}$, the relation gives $\omega_{sat} = 14.3, 11.1, 6.3\,\omega_\odot$, respectively, for the solid body models, and $\omega_{sat} = 11.9, 9.35, 5.61\,\omega_\odot$ for the differentially rotating models. The value for solar mass and solid body rotation is very close to the value of $14\,\omega_\odot$ we assumed earlier, as derived from the convective turnover time-scale, but at 0.8 and $0.5\,\mathrm{M_\odot}$, ω_{sat} is larger than the values of $8\,\omega_\odot$ and $3\,\omega_\odot$ predicted by equation (10): the slope of ω_{sat} as a function of mass is less steep than predicted from the convective turnover time-scale.
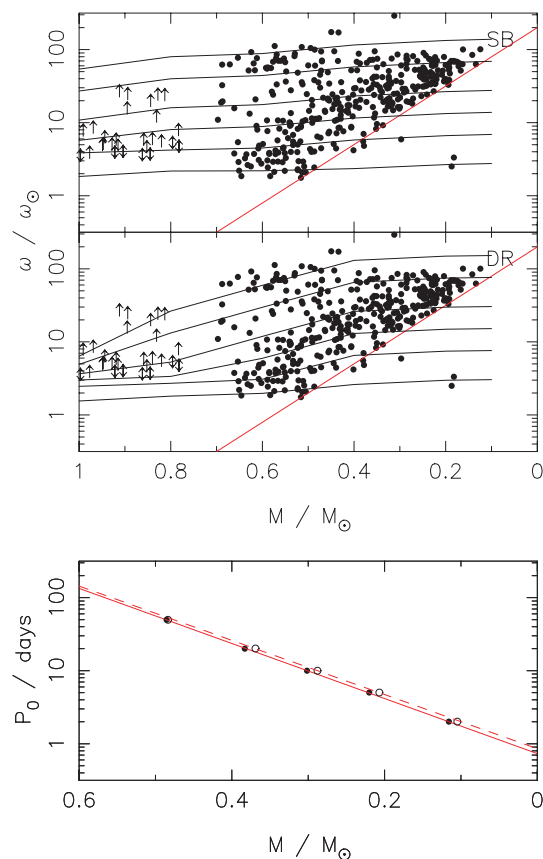
Figure 21. As Fig. 20, but for varying P_0, with fixed $t_{\rm disc} = 10\,{\rm Myr}$. The curves show the models for $P_0 = 1, 2, 5, 10, 20, 50\,{\rm d}$ (top to bottom).

The decrease of $\omega_{\rm sat}$ with decreasing mass, as determined in this work, effectively reduces the amount of angular momentum loss experienced by lower mass stars, compared to what would be experienced if the value was the same as at solar mass. This has also been seen in previous work e.g. Barnes & Sofia (1996).

6.2.5 Detailed evolution

Fig. 23 shows the results of attempting to evolve the measured rotation periods in NGC 2362 forward in time to the age of NGC 2516 using the models we have described, with the relations fit from Fig. 22 for $\omega_{\rm sat}$ as a function of mass, on an object-by-object basis. By doing this, we can test if the model we have presented can reproduce the observations of NGC 2516, given the NGC 2362 rotators as in input. Note that we have neglected disc locking in this analysis for simplicity.

The apparent mass-dependent morphology of the NGC 2516 distribution is well reproduced from the NGC 2362 distribution by the models, with two exceptions: for the slow rotators at the highest masses in the diagram, the predicted periods are too short by a factor of $\sim$2–3 compared to the observations for the solid body models, and slightly too short for the differentially rotating models. This suggests that slow rotators experience more angular momentum loss on the ZAMS than the models predict. Conversely, the solid body models provide a better fit to the fast rotators, especially in the mass range 0.6–0.8 $\rm M_{\odot}$. This is not surprising in light of the conclusions of Section 6.2.2.
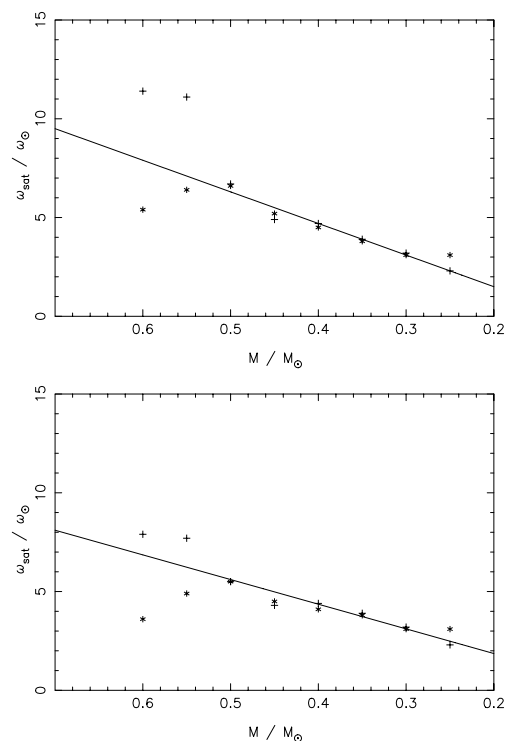

Figure 22. $\omega_{\rm sat}$ plotted as a function of mass, in 0.1-$\rm M_{\odot}$, bins, from fitting to the NGC 2516 j distribution lower 25 percentile (plus symbols) and upper 90 percentile (stars), using NGC 2362 as the initial condition, for solid body models (top) and differentially rotating models (bottom; $\tau_c = 1.0\,{\rm Gyr}$). This diagram indicates that a single functional form fails to fit all of these measures simultaneously for $M \gtrsim 0.5\,\rm M_{\odot}$, but that a simple linear relation is a good approximation at lower masses. The straight lines show a fit for $M \leqslant 0.5\,\rm M_{\odot}$, finding $(\omega_{\rm sat}/\omega_{\odot}) = 16.0(M/\rm M_{\odot}) - 1.7$ (solid body models) and $(\omega_{\rm sat}/\omega_{\odot}) = 12.5(M/\rm M_{\odot}) - 0.6$ (differentially rotating models).

In particular, the form of mass dependence for $M \lesssim 0.6\,\rm M_{\odot}$ is approximately correct, with the exception of a small number of objects rotating faster than the apparent 'limit' of $\sim$0.2 d seen in the NGC 2516 data. A small number of objects are also visible in the evolved NGC 2362 distribution above the $P \propto M^3$ relation seen for the slowest rotators in NGC 2516. Since these originated as relatively slow rotators in NGC 2362, we suspect that they are the result of field contamination, or errors in the measured rotation periods in that sample due to the limited time baseline of the observations.

This work suggests that the mass dependence of the observed rotation period distribution is reproduced by the combination of the initial conditions as seen in NGC 2362, the mass dependence of stellar contraction on the PMS, and the mass dependence of the saturation angular velocity $\omega_{\rm sat}$. Furthermore, the convergence in rotation rates as a function of time (see also Fig. 19) is explained reasonably well by saturation of the angular momentum losses, over the mass range of interest for NGC 2516, apparently without need to invoke any further effects.

Fig. 24 shows the same comparison for M34, showing that the feature of constant rotation period as a function of mass for $M \gtrsim 0.6\,\rm M_{\odot}$ is also well reproduced by the models, at approximately the correct period in the case of the differentially rotating models, and again at a shorter period than the observed value for the solid body models. It should be noted that the adopted values of $\omega_{\rm sat}$ in this mass range are not well constrained by the NGC 2516 data used to calibrate them, and have a strong effect on the morphology of this
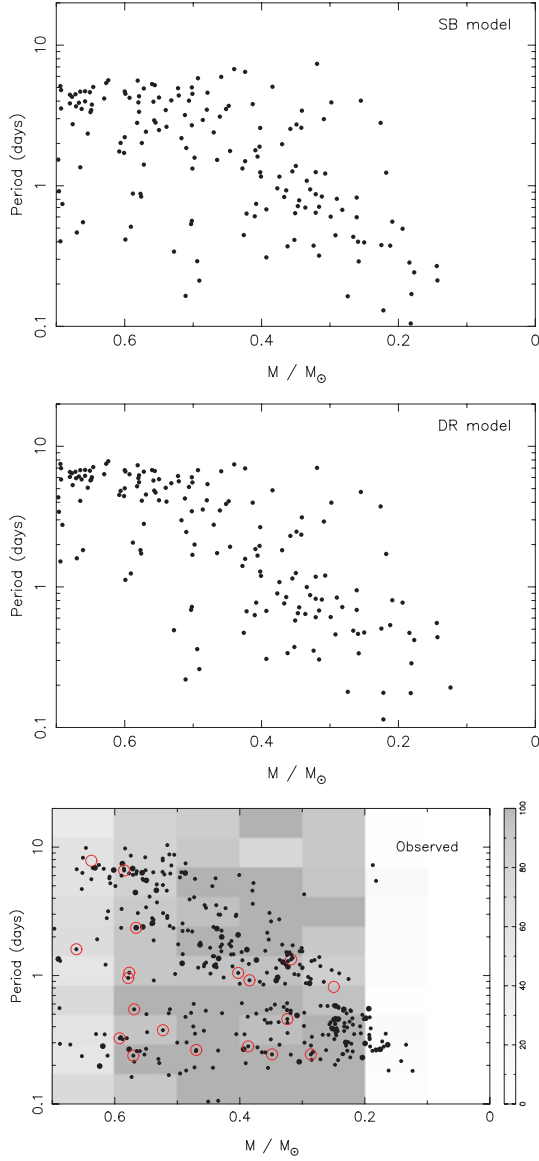
Figure 23. Rotation period as a function of mass, using the model presented in Section 6.2 to evolve the NGC 2362 distribution of Fig. 17 forward in time from 5 to 150 Myr for the solid body (upper panel) and differentially rotating (middle panel) models, and the observed NGC 2516 distribution for comparison (lower panel).

Figure 24. Rotation period as a function of mass, using the model presented in Section 6.2 to evolve the NGC 2362 distribution of Fig. 17 forward in time from 5 to 200 Myr for the solid body (upper panel) and differentially rotating (middle panel) models, and the observed M34 distribution for comparison (lower panel).

part of the diagram, so it is possible that any deviations here result from our assumption of a linear relation over the entire mass range.

7 CONCLUSIONS

We have reported on results of an *i*-band photometric survey of NGC 2516, covering ∼1 deg² of the cluster. Selection of candidate members in a *V* versus *V − I* CMD using an empirical fit to the cluster main sequence found 1685 candidate members, over a *V* magnitude range of 16 < *V* < 26 (covering masses from 0.7 M$_\odot$ down to below the brown dwarf limit). The likely field contamination level was estimated using a simulated catalogue of field objects from the Besançon Galactic models (Robin et al. 2003), finding that ∼650 objects were likely field contaminants, an overall contamination
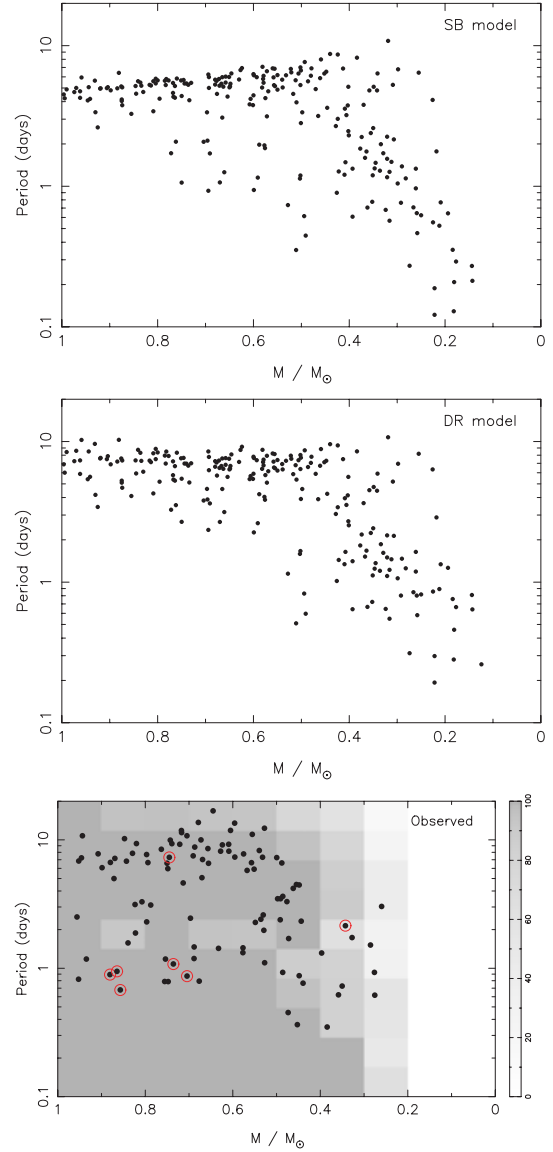
level of ∼39 per cent, implying that there are ∼1000 real cluster members over this mass range in our field of view.

From ∼8 nights of time-series photometry we derived light curves for ∼104 000 objects in the NGC 2516 field, achieving a precision of <1 per cent per data point over 15 ≲ *i* ≲ 19. The light curves of our candidate cluster members were searched for periodic variability corresponding to stellar rotation, giving 362 detections over the mass range 0.15 < *M*/M$_\odot$ < 0.7.

A striking morphology was found in the rotation period distribution as a function of both mass, with a median relation of $P \propto M^2$ (or constant specific angular momentum *j*) for masses below ∼0.6 M$_\odot$, with the slowest rotators (the majority of the sample) following $P \propto M^3$ ($j \propto M^{-1}$), with the fastest rotators over the entire mass range having $P \gtrsim 0.25$ d (corresponding to a line of $j \propto M^2$). Our earlier M34 results indicate that for $M \gtrsim 0.6$ M$_\odot$, the slowest

rotators follow instead $P \sim$ constant as a function of mass, with a transition between the two regimes at $M \sim 0.6\,M_{\odot}$. We suggest that this mass corresponds to the transition to convectively dominated stellar interiors moving to lower masses. This could be tested by examining rotation period distributions over a wider range of ages for M dwarfs.

In Section 6.2, simple models of the rotational evolution were considered, both for the solid body case, and including differential rotation between a decoupled radiative core and convective envelope, following Bouvier et al. (1997) and Allain (1998). A Kawaler (1988) angular momentum loss law incorporating saturation at a critical angular velocity ω_{sat} was assumed. The results indicate that a mass-dependent saturation velocity (e.g. of the form suggested by Sills et al. 2000) is required to reproduce the observations. Furthermore, we find that solid body rotation is sufficient to explain the evolution of the fastest rotators, but core-envelope decoupling appears to be needed to explain the evolution of the slowest rotators. This may indicate that the redistribution of angular momentum at the core/envelope boundary is more efficient in fast rotators. We were unable to find a model which fits both the fast and slow rotators simultaneously. Further, rotation period measurements at low masses, particularly for ages intermediate between 5 and 150 Myr and for ages >200 Myr, will provide more stringent constraints on the models, but the present observations already indicate the need for more theoretical work.

We intend to publish the final catalogue of NGC 2516 membership candidates after obtaining follow-up spectroscopy. However, the preliminary catalogue of membership candidates is available on request.

ACKNOWLEDGMENTS

REFERENCES

Aigrain S., Hodgkin S., Irwin J., Hebb L., Irwin M., Favata F., Moraux E., Pont F., 2007, MNRAS, 375, 29
Allain S., 1998, A&A, 333, 629
Allain S., Fernandez M., Martín E. L., Bouvier J., 1996, A&A, 314, 173
Balona L. A., Laney C. D., 1996, MNRAS, 281, 1341
Baraffe I., Chabrier G., Allard F., Hauschildt P. H., 1998, A&A, 337, 403
Barnes S., Sofia S., 1996, ApJ, 462, 746
Barnes J. R., Collier Cameron A., Unruh Y. C., Donati J. F., Hussain G. A. J., 1998, MNRAS, 299, 904
Barnes S. A., Sofia S., Prosser C. F., Stauffer J. R., 1999, ApJ, 516, 263
Basri G., Martín E. L., 1999, ApJ, 510, 266
Boesgaard A. M., Friel E. D., 1990, ApJ, 351, 467
Bouvier J., Forestini M., Allain S., 1997, A&A, 326, 1023
Bouwman J., Lawson W. A., Dominik C., Feigelson E. D., Henning Th., Tielens A. G. G. M., Waters L. B. F. M., 2006, ApJ, 653, 57
Chabrier G., Baraffe I., 1997, A&A, 327, 1039
Chabrier G., Baraffe I., Allard F., Hauschildt P. H., 2000, ApJ, 542, 464
Damiani F., Flaccomio E., Micela G., Sciortino S., Harnden F. R., Jr, Murray S. S., Wolk S. J., Jeffries R. D., 2003, ApJ, 588, 1009
Delfosse X., Forveille T., Perrier C., Mayor M., 1998, A&A, 331, 581
González J. F., Lapasset E., 2000, AJ, 119, 2296
Haisch K. E., Jr, Lada E. A., Lada C. J., 2001, ApJ, 553, 153
Herbst W., Bailer-Jones C. A. L., Mundt R., 2001, ApJ, 554, 197
Herbst W., Bailer-Jones C. A. L., Mundt R., Meisenheimer K., Wackermann R., 2002, A&A, 396, 513
Hillenbrand L., 1997, AJ, 113, 1733
Hodgkin S. T., Irwin J. M., Aigrain S., Hebb L., Moraux E., Irwin M. J., 2006, Astron. Nachr., 327, 9
Irwin M. J., Lewis J. R., 2001, New Astron., 45, 105
Irwin J., Aigrain S., Hodgkin S., Irwin M., Bouvier J., Clarke C., Hebb L., Moraux E., 2006, MNRAS, 370, 954
Irwin J., Irwin M., Aigrain S., Hodgkin S., Hebb L., Moraux E., 2007, MNRAS, 375, 1449
Jeffries R. D., James D. J., Thurston M. R., 1998, MNRAS, 300, 550
Jeffries R. D., Thurston M. R., Hambly N. C., 2001, A&A, 375, 863
Jones B. F., Prosser C. F., 1996, AJ, 111, 1193
Jones B. F., Fischer D. A., Stauffer J. R., 1996, AJ, 112, 1562
Kawaler S. D., 1998, ApJ, 333, 236
Kim Y. C., Demarque P., 1996, ApJ, 457, 340
Krishnamurthi A., Pinsonneault M. H., Barnes S., Sofia S., 1997, ApJ, 480, 303
Krishnamurthi A. et al., 1998, ApJ, 493, 914
Lamm M. H., Mundt R., Bailer-Jones C. A. L., Herbst W., 2005, A&A, 430, 1005
Landolt A. J., 1992, AJ, 104, L340
MacGregor K. B., 1991, in Catalano S., Stauffer J. R., eds, Angular Momentum Evolution of Young Stars. Kluwer, Dordrecht, p. 315
Magnitskii A. K., 1987, SvA, 13, L451
Makidon R. B., Rebull L. M., Strom S. E., Adams M. T., Patten B. M., 2004, AJ, 127, 2228
Martín E. L., Zapatero Osorio M. R., 1997, MNRAS, 286, L17
Mayor M., 1974, A&A, 32, 321
Meusinger H., Stecklum G., Reimann H. G., 1991, A&A, 245, 57
Meynet G., Mermilliod J.-C., Maeder A., 1993, A&AS, 98, 477
Moitinho A., Alves J., Huélamo N., Lada C. J., 2001, ApJ, 563, 73
Moraux E., Bouvier J., Clarke C., 2005, Astron. Nachr., 326, 985
Naylor T., Jeffries R. D., 2006, MNRAS, 373, 1251
O'Dell M. A., Collier Cameron A., 1993, MNRAS, 262, 521
O'Dell M. A., Hendry M. A., Collier Cameron A., 1994, MNRAS, 268, 181
O'Dell M. A., Hilditch R. W., Collier Cameron A., Bell S. A., 1996, MNRAS, 284, 874
Park B., Sung H., Bessell M., Kang Y., 2000, AJ, 120, 894
Patten B., Simon T., 1996, ApJS, 106, 489
Perryman M. A. C. et al., 1998, A&A, 331, 81
Pillitteri I., Micela G., Damiani F., Sciortino S., 2006, A&A, 450, 993
Pinfield D. J., Dobble P. D., Jameson R. F., Steele I. A., Jones H. R. A., Katsiyannis A. C., 2003, MNRAS, 342, 1241
Prosser C. F., 1991, PhD thesis, Univ. California, Santa Cruz
Prosser C. F., Randich S., 1998, Astron. Nachr., 319, 210
Prosser C. F., Schild R. E., Stauffer J. R., Jones B. F., 1993a, PASP, 105, 269
Prosser C. F. et al., 1993b, PASP, 105, 1407
Prosser C. F. et al., 1995, PASP, 107, 211
Prosser C. F., Randich S., Simon T., 1998, Astron. Nachr., 319, 215
Queloz D., Allain S., Mermilliod J.-C., Bouvier J., Mayor M., 1998, A&A, 335, 183

Radick R. R., Thompson D. T., Lockwood G. W., Duncan D. K., Baggett W. E., 1987, ApJ, 321, 459

Ramsay G., Harra L., Kay H., 2003, MNRAS, 341, 1388

Robin A. C., Reylé C., Derrière S., Picaud S., 2003, A&A, 409, 523

Scholz A., Eislöffel J., 2004a, A&A, 419, 249

Scholz A., Eislöffel J., 2004b, A&A, 421, 259

Sciortino S. et al., 2001, A&A, 365, 259

Sills A., Pinsonneault M. H., Terndrup D. M., 2000, ApJ, 534, 335

Skumanich A., 1972, ApJ, 171, 565

Soderblom D. R., Stauffer J. R., Hudon J. D., Jones B. F., 1993, ApJS, 85, 315

Stauffer J. R., Hartmann L. W., 1987, ApJ, 318, 337

Stauffer J. R., Hartmann L., Soderblom D. R., Burnham N., 1984, ApJ, 280, 202

Stauffer J. R., Hartmann L. W., Burnham J. N., Jones B. F., 1985, ApJ, 289, 247

Stauffer J. R., Schild R. A., Baliunas S. L., Africano J. L., 1987, PASP, 99, 471

Stauffer J. R., Hartmann L. W., Jones B. F., 1989, ApJ, 346, 160

Sung H., Bessell M. S., Lee B.-W., Lee S.-G., 2002, AJ, 123, 290

Terndrup D. M., Krishnamurthi A., Pinsonneault M. H., Stauffer J. R., 1999, AJ, 118, 1814

Terndrup D. M., Stauffer J. R., Pinsonneault M. H., Sills A., Yuan Y., Jones B. F., Fischer D., Krishnamurthi A., 2000, AJ, 119, 1303

Terndrup D. M., Pinsonneault M., Jeffries R. D., Ford A., Sills A., 2002, ApJ, 576, 950

Van Leeuwen F., Alphenaar P., Meys J. J. M., 1987, A&AS, 67, 483

Vilhu O., 1984, A&A, 133, 117

Wolk S. J. et al., 2004, ApJ, 606, 466

SUPPLEMENTARY MATERIAL

The following supplementary material is available for this article.

Table 1. Properties of our 362 rotation candidates. The period P in days, i-band amplitude α_i (units of magnitudes, in the instrumental bandpass), interpolated mass and radius (from the models of Baraffe et al. 1998, derived using the I magnitudes) are given (where available). Our identifiers are formed using a simple scheme of the cluster name, field number, CCD number and a running count of stars in each CCD, concatenated with dashes.

This material is available as part of the online paper from http://www.blackwell-synergy.com/doi/abs/10.1111/j.1365-2966.2007.11640.x (this link will take you to the article abstract).

Please note: Blackwell Publishing is not responsible for the content or functionality of any supplementary materials supplied by the authors. Any queries (other than missing material) should be directed to the corresponding author for the article.

This paper has been typeset from a TEX/LATEX file prepared by the author.